PROCEEDINGS A

rspa.royalsocietypublishing.org

Research

Article submitted to journal

Subject Areas:
Mathematical modelling, Applied mathematics

Keywords:
Pressure-driven growth, Fractional-flow theory, Foam improved oil recovery, Flow in porous media, Flow reversal, Method of characteristics

Author for correspondence:
P. Grassia
e-mail: paul.grassia@strath.ac.uk

THE ROYAL SOCIETY
PUBLISHING

Modelling Foam Improved Oil Recovery: Towards a Formulation of Pressure-Driven Growth with Flow Reversal

M. Eneotu[1], P. Grassia[1]

[1] Department of Chemical and Process Engineering, University of Strathclyde, James Weir Building, 75 Montrose Street, Glasgow G1 1XJ, UK

The pressure-driven growth model that describes the 2-D propagation of a foam through an oil reservoir is considered as a model for surfactant-alternating-gas improved oil recovery. The model assumes a region of low mobility, finely-textured foam at the foam front where injected gas meets liquid. The net pressure driving the foam is assumed to reduce suddenly at a specific time. Parts of the foam front, deep down near the bottom of the front, must then backtrack, reversing their flow direction. Equations for 1-D fractional flow, underlying 2-D pressure-driven growth, are solved via the method of characteristics. In a diagram of position vs time, the backtracking front has a complex double fan structure, with two distinct characteristic fans interacting. One of these characteristic fans is a reflection of a fan already present in forward flow mode. The second fan however only appears upon flow reversal. Both fans contribute to the flow's Darcy pressure drop, the balance of the pressure drop shifting over time from the first fan to the second. The implications for 2-D pressure-driven growth are that the foam front has even lower mobility in reverse flow mode than it had in the original forward flow case.

1. Introduction

During oil and gas production, typically only a fraction of the oil available in a reservoir can be extracted under the reservoir's own pressure. After that, fluids must be injected into the reservoir to displace the remaining oil, the direction of displacement then being from an injection well towards one or more production wells. Although various different choices of injection fluids can

be made [1–5] (e.g. water injection, steam injection, carbon dioxide injection, polymer injection, etc.), one promising candidate displacing fluid is foam [6–9], the injection process then being termed "foam improved oil recovery" or foam IOR.

One of the reasons why foam works so effectively in applications such as these is that it tends to have very low mobility [8] when moving through porous media such as oil reservoirs. This low mobility helps to suppress so called "fingering instabilities" [10] that would arise when higher mobility fluids are injected. Such fingering instabilities are undesirable in the context of foam IOR since they cause injected fluid to flow along a small selection of high permeability preferred flow paths bypassing much of the reservoir fluid originally in place. Using a low mobility injection fluid such as foam avoids this situation by allowing oil to be displaced more uniformly [11], even to the point that foam is diverted preferentially into low permeability strata which have previously been left unswept [12–14]. Indeed, as the fluid present with the lowest mobility, foam tends to control the flow of all the other reservoir fluids. It then follows that if the flow of foam can be controlled, the evolution of the entire displacement process to recover oil can also be controlled.

In view of this, it is unsurprising that there have been many studies trying to understand and/or model [15–26] how foam behaves when flowing through porous media. Models cover the full range of scales from small scale, i.e. motion of individual foam films within individual pore spaces [27–33] to larger scale, i.e. foam front displacement through a porous medium as a whole [18,19,23,24,26] up to a very large scale, i.e. an entire reservoir [20,34–39]. The smaller scale models mentioned above incorporate a high level of geometric microstructural detail. Larger scale models are unable to include all this small scale detail. Nevertheless processes occurring at one scale still manage to feed information into models at a yet larger scale.

This work is concerned with a particular reservoir scale model called "pressure-driven growth" [40–42] and a porous medium model that underlies it (so called "fractional-flow theory" [43–46]) and which feeds information to it. Pressure-driven growth in particular is used to describe a specific type of foam IOR, namely surfactant-alternating-gas or SAG [34,37,38,40,47], in which slugs of liquid surfactant solution are injected into a reservoir alternating with slugs of gas: foam is formed in situ as the injected gas meets the surfactant solution. Pressure-driven growth can be considered in 2-D (one vertical and one horizontal coordinate) or 3-D (one vertical and two horizontal coordinates): we treat the 2-D formulation here, since the generalisation of the pressure-driven growth model to 3-D is straightforward [40]. The underlying fractional flow meanwhile is formulated in 1-D.

Pressure-driven growth (in 2-D) has been used to describe a number of foam IOR scenarios in reservoirs including effects of reservoir heterogeneity [48] and anisotropy [49,50], the influence of surfactant migrating downward through a reservoir [51], and also the effect of an increase in injection pressure used to drive the foam along [52]. There is however a scenario that pressure-driven growth has not yet tackled successfully, namely a *decrease* in net driving pressure moving the foam along, net driving pressure here being the difference between an injection pressure and a pressure downstream of the displacing foam.

Although in oil recovery terms it is best to keep injection pressure as high as possible [52], a decrease could conceivably still occur for a number of scenarios e.g. a reduction in performance of a pump delivering injection fluids to foam IOR or else a deliberate reduction in injection pressure to prevent fracturing rock. A well might also need to be shut in (i.e. injection ceased): the seal placed on a such a well would need to withstand a pressure high enough to prevent the shut-in well from collapsing, but even so, not quite so high as the pressure that would have been needed to continue injection outwards from it. It is also conceivable (albeit again not necessarily desirable in oil recovery terms) that net driving pressure for foam could decrease, not due to a decrease in injection pressure upstream, but rather due to a rise in pressure downstream, close to a production well say. This could happen e.g. if an additional injection well were to be brought online in a neighbouring part of the reservoir, driving fluids towards that same production well, and leading to changes in an overall pressure field.

In scenarios like these, over much the flow domain, foam continues to displace reservoir fluids from the original injection well towards the original production well, albeit less rapidly than before. However there is an effect of hydrostatic pressure which must be taken into account: foam is less dense than fluids present in the reservoir downstream (e.g. oil, water, previously injected slugs of surfactant solution) and this density difference produces a hydrostatic pressure field [40]. As a result, there is a certain "neutral" depth at which the hydrostatic pressure (downstream) balances injection pressure (upstream) leading to zero net driving pressure: foam cannot penetrate any deeper than this [41]. If injection pressure falls and/or downstream pressure rises, this maximum penetration depth (or "neutral" depth) shifts upwards. Foam that penetrated down to the original neutral depth now has an unbalanced hydrostatic pressure pushing it back upwards: i.e. foam at depth must undergo a flow reversal, even though foam higher up continues propagating in the original flow direction.

In scenarios of injection continuing at a reduced net driving pressure, the reverse flow at depth on the foam front will generally be less than the forward flow higher up, although for a shut-in well mentioned earlier (i.e. no net injection), the reverse flow at depth and forward flow higher up must balance. Either way, flow reversal is the phenomenon we model here. Outright reversal can be viewed as an extreme case of a more general change in direction of flow due to a change in the driving pressure field. We need to understand such flow direction changes, and flow reversal in particular, in order to know how the totality of fluids distribute in this system, even though admittedly in oil recovery applications, the flow-reversed part of the front at depth should contain rather less oil than the forward flowing part that we continue to recover higher up. This follows because (as mentioned earlier) it is advantageous to inject at as high a pressure as possible [52], meaning that, by design, foam already penetrates rather deeper than the majority of oil is likely to be present. Hence shifting the "neutral depth" upwards a little does not change this situation.

In the context of pressure-driven growth, flow reversal is known to be numerically challenging to model. The reason is that pressure-driven growth is well-behaved numerically when a foam front that is displacing through the reservoir is convex (seen from the direction towards which it is advancing, see e.g. the front sketched in Figure 1(a)) but is ill-behaved numerically for parts of the front that are concave [41]: concavities can focus down into sharp corners at which the front reorients significantly over a small distance. If however the flow direction of at least part of the foam front reverses as we envisage here, an originally convex section of front switches to being concave (viewed from the new direction towards which it is now advancing, see Figure 2(a)).

Fortunately strategies exist for regularising the numerical behaviour of concave fronts within pressure-driven growth [41], and these can be invoked here. There is however an even more fundamental issue that we face. As has been mentioned, the pressure-driven growth model was formulated [40] based on an underlying fractional-flow theory, which informs the pressure-driven growth model, i.e. feeds parameters to it. However the formulation as it currently stands [40,41] assumes forward-directed fractional flows. A complete reformulation of pressure-driven growth turns out to be required for a situation with an initial forward flow followed by a flow reversal: carrying out this reformulation is the main novel contribution that the present work achieves. This is done, as one might expect, by returning to fractional-flow theory, obtaining novel solutions for the equations governing that theory under flow reversal, and then obtaining parameters to feed back into pressure-driven growth. A key result from doing this will be that a flow-reversed foam front is much less mobile than the original forward flowing front was.

The rest of this work is laid out as follows. Section 2 sets the geometrical context of the study and outlines the main findings to be presented. Section 3 provides parameter values to use in foam IOR models, including a base case parameter set. Section 4 presents governing equations and works through an example, presenting results to illustrate the system behaviour: the results build towards the reformulation of pressure-driven growth incorporating flow reversal conditions. Section 5 then concludes the work. The supplementary material explores the extent to which model results are sensitive to chosen parameter values, varying with respect to the base case.

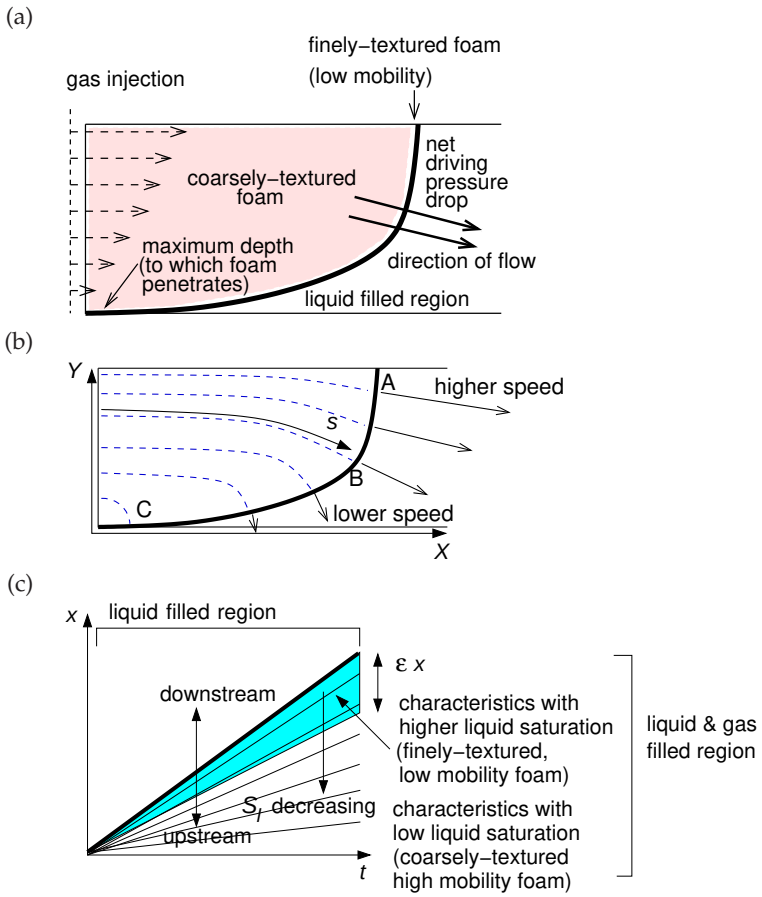

Figure 1. (a) Schematic sketch of 2-D pressure-driven growth. Gas injection causes a foam front to propagate, with finely-textured, low mobility foam at the front separating liquid (downstream) from coarsely-textured foam (upstream). The direction of propagation is normal to the front, and the speed of propagation depends on a net pressure difference (the difference between an upstream injection pressure and a downstream hydrostatic pressure). There is a "neutral" depth at which these two pressures balance, hence giving the maximum depth to which foam can penetrate. (b) Coordinate system (X, Y) for pressure-driven growth showing the current front shape for some arbitrary time τ. Different points on the front have followed different trajectories (dashed curves) to reach their current location (the variable s measures the path length on each trajectory, and the thickness of the front is assumed to be εs for some given $\varepsilon \ll 1$). The height of a point above the neutral depth determines its current speed (indicated by arrows), so that e.g. point A is moving faster than B, whereas point C (which has nearly reached the neutral depth) is barely moving. (c) Sketch of 1-D fractional flow x-t diagram (the variable x here is the 1-D analogue of the path length variable s in 2-D pressure-driven growth, and t is time). A foam front (bold line) separates liquid downstream from liquid and gas (i.e. foam) upstream. In the upstream liquid and gas filled region, a fan of characteristics appears (each characteristic line of fixed liquid saturation S_l and with specified slope). The lowest mobilities in the fan correspond to S_l values close to the front (shaded region), the width of this region at any time t being a fraction ε of the distance x through which the front has propagated.

2. Context and findings of the present study

The 2-D pressure-driven growth model [40,41] involves tracking elements on a foam front executing curved trajectories, with different elements (e.g. points A, B and C in Figure 1(b)) displacing through different path lengths s. Pressure-driven growth only attempts to track finely-textured foam formed in situ located at the front itself [40]. This has a specific liquid saturation,

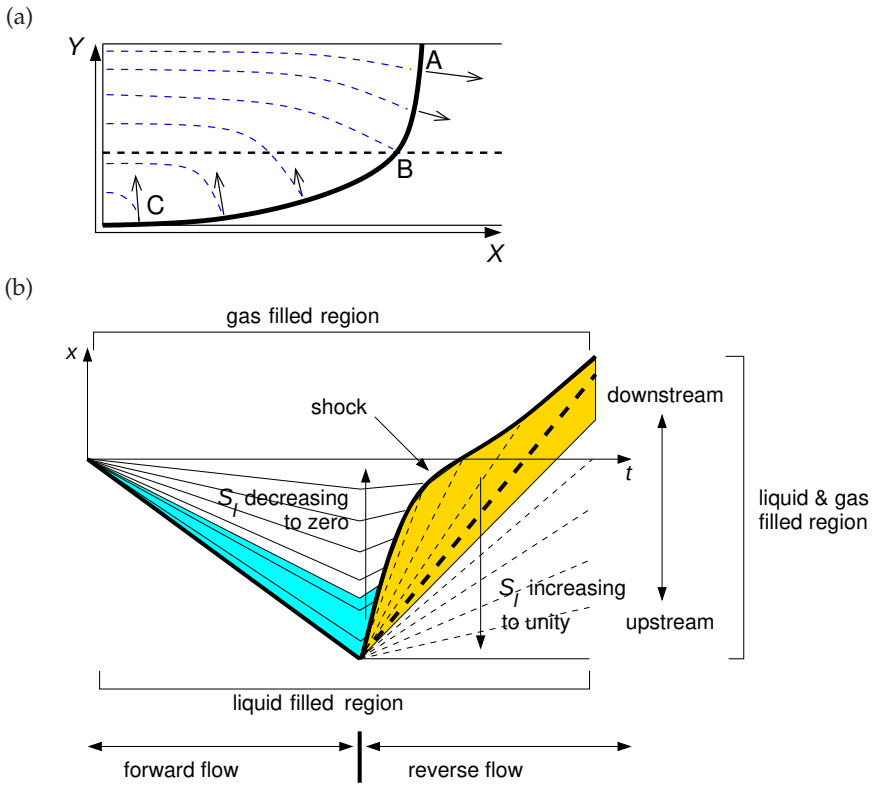

Figure 2. (a) Schematic sketch of pressure-driven growth admitting flow reversal. Initially pressure-driven growth proceeds in a forward direction, with points on the front following the paths indicated by the dashed curves. At a certain time, the injection pressure driving the flow is reduced, meaning that the "neutral" depth at which injection pressure balances hydrostatic pressure (indicated by a bold dashed line) shifts higher up than before. Points that are even higher up than this (e.g. the point labelled A) continue moving in much the same direction as before, albeit with a reduced net driving pressure and hence a reduced velocity. Points at the neutral depth (point B) cease moving altogether. Points even lower down (point C) move in the reverse direction from before: these are the points of interest here. (b) x-t diagram illustrating the predictions of fractional-flow theory under a forward flow followed by reverse flow: the sign convention adopted here is that forward flow corresponds to the negative x direction and reverse flow corresponds to the positive x direction. A characteristic fan appears during the forward flow phase, and this fan is reflected at the instant of flow reversal. However at the instant of flow reversal, a second characteristic fan appears. This corresponds to a different set of liquid saturations S_l (typically higher S_l values than the original fan). The two fans meet across a shock. On both fans there are certain subsets of S_l values that have low mobility (shown as shaded regions here). The bulk of the pressure drop occurs across these low mobility regions.

with saturation governing texture [43]: a minimum liquid saturation is required for foam to resist capillary collapse and thereby preserve a fine texture. Based on its fine texture, foam at the front is also expected to have low mobility, as it is the foam films that reduce mobility [19]. However moving back or forward from the foam front along the 2-D curved paths indicated in Figure 1(b), we encounter a different set of liquid saturations, and hence a different set of textures and mobilities. The mobility, or more specifically a quantity to be defined later called total relative mobility $\mathcal{M}_{\rm tot}$, is a function of liquid saturation S_l here, this function then capturing in an implicit fashion [24,26,53] the link between mobility and foam texture as well as that between texture and liquid saturation. The distribution of liquid saturations (and hence distribution of relative mobilities) moving back or forward along the 2-D curved paths, is assumed to be the same as

what would result from 1-D fractional-flow theory [43–46] using a "straightened out" 1-D path displaced through the same path length. This is illustrated in Figure 1(c), using now x to denote the 1-D spatial coordinate (as opposed to the 2-D path length s). Fractional-flow theory yields a so called fan of characteristic lines, giving the spatial distribution of S_l (and hence the spatial distribution of $\mathcal{M}_{\rm tot}$) for any specified front displacement x (or equivalently, for any specified time t, since we can use the 1-D fluid flux to relate x and t). Given the 1-D front location x, the 1-D fractional-flow theory can be used to identify a region adjacent to the front at which liquid saturations give low mobilities (low $\mathcal{M}_{\rm tot}$), the extent of this region being denoted εx in Figure 1(c). This information is then fed into 2-D pressure-driven growth.

The above discussion however, whether for 2-D pressure-driven growth or 1-D fractional flow, only concerns forward flows. What happens in 2-D under a possible reverse flow is illustrated in Figure 2(a). Points A, B and C in Figure 2(a) (analogous to points already shown in Figure 1(b)) behave differently after a reduction of injection pressure say. As mentioned earlier, the "neutral" depth at which the front does not displace moves higher up than before (to the bold dashed line in Figure 2(a)), so is above where the bottom of the front was originally. Point A remains above the new neutral depth so continues moving in the same direction as originally, albeit with a lesser speed due to the net driving pressure being reduced. Point B however finds itself exactly at the new neutral depth, so ceases to move altogether. Point C however is now below the neutral depth, so undergoes reverse flow: 1-D fractional flow incorporating reverse flow must then be used to find the mobility associated with a point such as C. This is what the present work achieves. Note that (unlike in 1-D) there is no requirement in a 2-D model, for a point such as C to retrace exactly the same (X, Y) positions during reverse flow that it passed through during forward flow. Indeed the 2-D model that we will develop does not require paths to be retraced: the 1-D fractional flow information that feeds into mobility of the 2-D model be will formulated in terms of distances travelled in forward and reverse flow, rather than full details of the 2-D layout of a trajectory.

Although we will present our detailed model and results in due course, it is useful to state in advance the main findings to be obtained. These are summarised schematically in Figure 2(b).

Supposing that the forward flow mode is now considered to proceed in the negative x direction (a contrast from Figure 1(c)), the reverse flow mode in Figure 2(b) proceeds in the positive x direction. The characteristic pattern during the forward flow phase is the same as in Figure 1(c), apart from the sign change for x. Upon flow reversal, we will find that the characteristic fan is reflected and starts to close up on itself in the x-t plane as Figure 2(b) shows. The size of the low mobility region (the shaded region on the reflected fan) should then be proportional to the difference between the distance propagated during the forward and reverse flow phases.

This is however not the full story. A second characteristic fan in Figure 2(b) appears at the instant of flow reversal, corresponding to different set of liquid saturations, typically higher saturations than those in the original fan. This new fan also has (see shaded region) a set of saturations with low mobility (albeit different mobility from that in the original fan). Moreover the spatial extent of this low mobility region starts out small and grows over time, whereas the extent of the low mobility region in the reflection of the original fan is now shrinking over time.

Which of the two low mobility regions ultimately accounts for the bulk of the pressure drop for a given imposed fluid flux (and thereby which of them ultimately determines the flux for a given imposed driving pressure difference) depends on how their mobilities and spatial extents compare. It turns out moreover that, taken separately, the two fans would occupy overlapping regions in the x-t plane. The system resolves this overlap as Figure 2(b) shows, by introducing a shock, with the reflected original fan being downstream of the shock and the new fan being upstream of it. Since the flow has reversed, the sense of what is meant by "downstream" and "upstream" has of course switched, i.e. gas is downstream now and liquid is upstream.

All of these features will be revealed by the 1-D fractional flow analysis to follow. Ultimately the 1-D fractional-flow theory will enable us to set up a 2-D pressure-driven growth model accounting for forward and reverse flow. Here however our aim is merely to set up the 2-D model in a well-posed fashion consistent with 1-D fractional flow. Solution of the 2-D model

μ_l/μ_g	$S_{l,*}$	$S_{l,\epsilon}$	R_f
10	0.37	0.02	185

Table 1. Set of parameter values to be used in base case calculations.

itself (incorporating reverse flow effects) is left for future work. Our purpose in the sections that follow is to show an actual calculation illustrating the principles for forward and reverse flow outlined above and as sketched in Figure 2(b). Before we can do that however we need to specify the parameter set with which we work: this is done in the next section.

3. Parameter set for fractional flow

This section defines the parameters needed to set up 1-D fractional-flow theory, and is laid out as follows. Section (a) specifies so called relative permeabilities, whilst section (b) specifies liquid and gas viscosities and also relative mobilities of liquid and gas. Both of the above sections assume the absence of foam, the effect of foam being considered in section (c). Fractional flow itself and total relative mobility are introduced in section (d).

(a) Relative permeabilities

The main parameters we require are relative permeabilities of liquid ($k_{r,l}$) and of gas (in the first instance in an unfoamed system, and denoted $k^0_{r,g}$). Both of these are functions of liquid saturation S_l, and, describe the flow of each phase through a given porous medium under multiphase flow conditions, relative to what would occur for single phase flow.

Typically [54] there is some irreducible liquid saturation at which no liquid can no longer flow, thereby setting a minimum level for S_l. Likewise there is an irreducible gas saturation and this sets a maximum level for S_l. Here, in the interests of simplicity, we assume these irreducible saturations are negligible, so that S_l can in principle cover the full domain $0 \leq S_l \leq 1$. This assumption is not too restrictive: even when irreducible saturations are non-negligible, it is possible to replace S_l by an "effective" liquid saturation [54] that does cover the domain 0 to 1. The theory with negligible irreducible saturations is thereby recovered.

Following [54,55] we assume power law relations for $k_{r,l}$ and $k^0_{r,g}$. For simplicity, we will assume throughout most of this work quadratic relations which illustrate behaviour

$$k_{r,l} = S_l^2, \quad k^0_{r,g} = (1 - S_l)^2. \tag{3.1}$$

It is possible to consider different powers, as has done by [35] based on data of [56]. The effect of considering different powers will be considered in the supplementary material.

(b) Viscosities and relative mobilities

We also require viscosities of liquid μ_l and gas μ_g phases, or more specifically (when we express the system in dimensionless form) the ratio between these viscosities. Relative mobilities of the liquid and (unfoamed) gas phases are respectively $\lambda_{r,l} \equiv k_{r,l}/\mu_l$ and $\lambda^0_{r,g} \equiv k^0_{r,g}/\mu_g$. Data provided by [40] for a SAG process suggests (unfoamed) gas is between one and two orders of magnitude less viscous than aqueous liquid (surfactant solution in the case of SAG). In this context it is worth remembering that oil reservoirs tend to be at elevated temperatures and pressures compared to surface conditions, and that can impact on the liquid-to-gas viscosity ratio. In what follows we assume that the ratio μ_l/μ_g is equal to 10 throughout (see Table 1).

(c) Effect of foam upon gas flow

So far we have considered a system without foam. In the presence of foam, liquid relative permeability $k_{r,l}$ and liquid relative mobility $\lambda_{r,l}$ are considered to be unchanged whereas gas relative permeability $k_{r,g}$ is reduced [40], possibly quite substantially. Viscosities μ_l and μ_g are assumed unchanged. Supposing that foam reduces gas relative permeability alone is a convenient assumption, albeit a simplification, given that in general foam could produce an increase in gas apparent viscosity in addition to a decrease in relative permeability. However the effect of foam increasing apparent viscosity is similar to the effect of foam decreasing relative permeability: in both cases relative mobility of gas $\lambda_{r,g} \equiv k_{r,g}/\mu_g$ decreases, typically quite substantially.

Data for effects of foam upon $k_{r,g}$ are available from [56] and a number of studies [23,26,35,43, 44,57] have fit parameters to such data. Studies typically define three parameters: R_f a maximum mobility reduction factor (a value in excess of unity); $S_{l,*}$ a liquid saturation at which a so called limiting capillary pressure is reached; and $S_{l,\epsilon}$ a range of liquid fractions about $S_{l,*}$ over which foam collapse occurs. Here we represent the foamed $k_{r,g}$ in terms of these parameters as

$$k_{r,g} = k^0_{r,g}\left(1 + (R_f - 1)\frac{(1 + \tanh((S_l - S_{l,*})/S_{l,\epsilon}))}{2}\right)^{-1}. \tag{3.2}$$

We choose (see Table 1) $S_{l,*} = 0.37$ in line with [43] and also $S_{l,\epsilon} = 0.02$ corresponding to a 2% progressive collapse [40] either side of $S_{l,*}$. It is clear from equation (3.2) that $k_{r,g}$ falls from $k^0_{r,g}$ for S_l less than about $S_{l,*} - O(S_{l,\epsilon})$ (the foam undergoes capillary collapse as it dries out in this regime [23,25] so becomes coarsely-textured and comparatively mobile) to a smaller value $k^0_{r,g}/R_f$ for S_l greater than about $S_{l,*} + O(S_{l,\epsilon})$ (so called strong foam [43,58] with fine texture and low gas mobility).

Other functional forms are possible [24] in lieu of equation (3.2). For instance [23,26,57] have used an $\arctan$ form rather than a $\tanh$ form, but the effect is the same: $k_{r,g}$ falls smoothly from $k^0_{r,g}$ to $k^0_{r,g}/R_f$ as S_l increases through $S_{l,*}$. Meanwhile [35,43,44] have assumed a straight line relation between $k^0_{r,g}/k_{r,g}$ and S_l over the domain $S_{l,*} - S_{l,\epsilon} \le S_l \le S_{l,*} + S_{l,\epsilon}$ with constant $k^0_{r,g}/k_{r,g}$ either side of this domain. This is slightly less convenient because the function $k_{r,g}$ is not smooth at $S_l = S_{l,*} \pm S_{l,\epsilon}$. This is the reason we choose a smooth function like equation (3.2).

Typically R_f values are very large, up to the order of tens of thousands [23,26,44,57] meaning that gas in foam is much less mobile than unfoamed gas. For example [43] used $R_f = 18500$. We will present some results with that R_f value later on towards the end of this work (see also supplementary material). For the most part however we will illustrate calculations with a smaller value $R_f = 185$ (see Table 1). Although not on the order of tens of thousands, this is still much larger than unity, so foam is still having a very significant effect on reducing the mobility of gas.

(d) Definition of fractional flow and total relative mobility

If a pressure gradient ∇p is applied, the superficial liquid flow down that pressure gradient is $-k\lambda_{r,l}\nabla p \equiv -(kk_{r,l}/\mu_l)\nabla p$ whilst superficial gas flow is $-k\lambda_{r,g}\nabla p \equiv -(kk_{r,g}/\mu_g)\nabla p$. The fraction of flow that is liquid f_l is therefore

$$f_l = \frac{\lambda_{r,l}}{\lambda_{r,l} + \lambda_{r,g}} = \frac{k_{r,l}/\mu_l}{k_{r,l}/\mu_l + k_{r,g}/\mu_g} \tag{3.3}$$

with $1 - f_l$ being the fraction of flow that is gas. Equation (3.3) can also be written as $f_l = k_{r,l}/(\mu_l \mathcal{M}_{\rm tot}) = k_{r,l}/M_{\rm tot}$ where $\mathcal{M}_{\rm tot}$ denotes the total relative mobility

$$\mathcal{M}_{\rm tot} = \lambda_{r,l} + \lambda_{r,g} = k_{r,l}/\mu_l + k_{r,g}/\mu_g, \tag{3.4}$$

with dimensionless analogue $M_{\rm tot} \equiv \mu_l \mathcal{M}_{\rm tot} = k_{r,l} + (\mu_l/\mu_g)k_{r,g}$.

Plots of f_l and $M_{\rm tot}$ vs S_l are given in Figure 3, for cases both without and with foam. In Figure 3(a), f_l without foam increases gradually from 0 to 1 as S_l increases. With foam the increase in f_l is more abrupt, and happens around $S_l = S_{l,*}$. Meanwhile $M_{\rm tot}$ without foam (see

Figure 3(b)) tends to decrease with increasing S_l although there is a small increase close to $S_l = 1$. By construction $M_{\rm tot}$ takes the value μ_l/μ_g (equal to 10 for our data) at $S_l = 0$ and equals unity at $S_l = 1$. With foam, $M_{\rm tot}$ falls abruptly in the neighbourhood of $S_{l,*}$, attaining (see Figure 3(c)) $M_{\rm tot}$ values much smaller than are achieved at either $S_l = 0$ or $S_l = 1$. As section 2 states, the basis of the pressure-driven growth model is that finely-textured, strong foam with sufficient liquid saturation to avoid capillary collapse has much lower mobility than either low liquid saturation foam (which has already collapsed to a coarsely-textured state) or pure liquid. One issue we will return to later however is that it is not clear whether the system necessarily selects the set of liquid saturations needed for this low mobility condition to be realised, at least not long as forward flow conditions (i.e. gas pushing into liquid) persist.

4. Governing equations and illustrative example

Having specified a parameter set, we now formulate and solve models, which we do as follows. Sections (a)–(b) present respectively the standard 2-D pressure-driven growth and 1-D fractional-flow theory in forward flow mode. Sections (c)–(d) then consider 1-D fractional-flow theory after reverse flow is imposed. Sections (e)–(f) relate 1-D fractional flow fluxes to driving pressures in the case of forward and reverse flows. Finally section (g) uses results from all the foregoing sections to derive equations describing 2-D pressure-driven growth under flow reversal.

(a) Pressure-driven growth: Forward flow case

In the first instance we consider pressure-driven growth in forward flow mode. A net driving pressure difference ΔP is imposed across a low mobility foam front of thickness εs, with s denoting the distance the front has displaced and ε being the ratio between front thickness and front displacement ($\varepsilon \ll 1$ here). The implication (already suggested in section 2 in the context of discussing Figure 1) is that any pressure drop occurs across a thin region of extent much smaller than the distance the front has displaced, albeit with the size of the region εs assumed proportional to the displacement distance s: in [41], a value $\varepsilon = 0.01$ was assumed for instance. We use P to denote pressure here (instead of p used earlier) to make a distinction between pressure-driven growth and fractional-flow theory. The pressure gradient at the front is $\nabla P = -(\Delta P/(\varepsilon s))\boldsymbol{n}$ where $\boldsymbol{n}$ is the front normal for an element of front.

Darcy's law then implies that the superficial gas flux at the front is $(k\lambda_{r,g}\Delta P/(\varepsilon s))\boldsymbol{n}$ where k is the permeability of the medium and $\lambda_{r,g} \equiv k_{r,g}/\mu_g$ is the relative mobility of (foamed) gas. The value of $\lambda_{r,g}$ depends on liquid saturation at the front S_l. We denote this saturation $S_{l,\rm fwd}$ to remind us that it is the saturation at the front in forward flow.

The foam front position $\boldsymbol{X}$ versus time τ is now assumed to propagate at the interstitial velocity of the gas, and hence for a medium of porosity ϕ becomes [41]

$$\frac{{\rm d}\boldsymbol{X}}{{\rm d}\tau} = \frac{k\lambda_{r,g}\Delta P}{(1 - S_{l,\rm fwd})\phi\varepsilon s}\boldsymbol{n}. \tag{4.1}$$

Again the choice of notation $\boldsymbol{X}$ and τ (instead of x and t used earlier) is deliberate to highlight the difference between pressure-driven growth and fractional flow.

Using the definitions from section 3(d) it is possible to express fractional flow of liquid f_l as $\lambda_{r,l}/\mathcal{M}_{\rm tot}$ and fractional flow of gas $1 - f_l$ as $\lambda_{r,g}/\mathcal{M}_{\rm tot}$. It then follows that

$$\frac{{\rm d}\boldsymbol{X}}{{\rm d}\tau} = \frac{k\mathcal{M}_{\rm tot,fwd}\Delta P}{\phi\varepsilon s}\frac{(1 - f_{l,\rm fwd})}{(1 - S_{l,\rm fwd})}\boldsymbol{n} \equiv \frac{q}{\phi}\frac{(1 - f_{l,\rm fwd})}{(1 - S_{l,\rm fwd})}\boldsymbol{n} \tag{4.2}$$

where $q \equiv k\mathcal{M}_{\rm tot,fwd}\Delta P/(\varepsilon s)$ is (by Darcy's law) the magnitude of the total fluid flux (liquid and gas taken together), and where $\boldsymbol{q} \equiv q\,\boldsymbol{n}$ is the vector flux. Moreover $\mathcal{M}_{\rm tot,fwd}$ and $f_{l,\rm fwd}$ are specifically total mobilities and fractional flow at the saturation $S_l = S_{l,\rm fwd}$.

Note that ΔP and hence q here depend on where we are on the front. To compute ΔP, the injection pressure driving the front denoted $P_{\rm inj}$ is opposed by a hydrostatic pressure, which

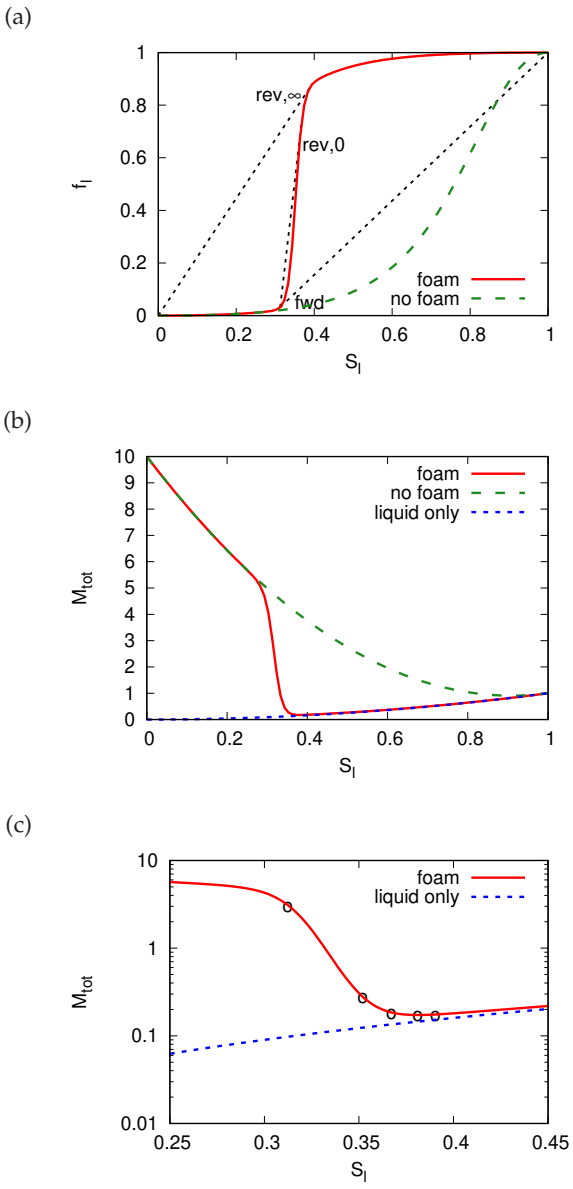

Figure 3. (a) Fractional flow curve f_l vs liquid saturation S_l, comparing the case with foam and the no foam case. In the case with foam, three lines are constructed on the fractional flow curve which are (from right to left), a line joining $(S_{l,\mathrm{fwd}}, f_l(S_{l,\mathrm{fwd}}))$ to (1,1); a line joining $(S_{l,\mathrm{fwd}}, f_l(S_{l,\mathrm{fwd}}))$ to $(S_{l,\mathrm{rev},0}, f_l(S_{l,\mathrm{rev},0}))$; and a line joining (0,0) to $(S_{l,\mathrm{rev},\infty}, f_l(S_{l,\mathrm{rev},\infty}))$. (b) Total mobility curve M_{tot} vs liquid saturation S_l comparing the case with foam and the no foam case. Also shown is the mobility of liquid $\lambda_{r,l}$ suitably non-dimensionalised ($\mu_l \lambda_{r,l} \equiv f_l M_{\mathrm{tot}}$ i.e. the contribution to M_{tot} coming from the liquid). (c) Zoomed view of total mobility curve on log scale. The circled points correspond (from left to right) to mobilities at S_l values $S_{l,\mathrm{fwd}}$, $S_{l,\mathrm{infl}}$, $S_{l,\mathrm{rev},0}$, $S_{l,\mathrm{min\ mob}}$, $S_{l,\mathrm{rev},\infty}$.

grows with depth with a gradient $\Delta\rho\, g$ where $\Delta\rho$ is the density difference between liquid and gas, and g is gravity acceleration. We now make both $\boldsymbol{X}$ and s dimensionless on a scale $P_{\rm inj}/(\Delta\rho\, g)$ (physically a maximum penetration depth or "neutral" depth for forward flow), whilst ΔP is made dimensionless on the scale $P_{\rm inj}$. Meanwhile time τ is made dimensionless on a scale

$$\tau_{\rm scale} = \frac{\phi\varepsilon P_{\rm inj}}{k\mathcal{M}_{\rm tot,fwd}\Delta\rho^2 g^2}\frac{(1-S_{l,\rm fwd})}{(1-f_{l,\rm fwd})}. \tag{4.3}$$

For compactness of notation we use the same symbols $\boldsymbol{X}\equiv(X,Y)$, s, ΔP and τ to denote both dimensional and dimensionless variables: note that from here on, we work primarily with equations in terms of dimensionless variables, although we revisit dimensional variables briefly in sections (e) and (g) below. The (dimensionless) model becomes

$$\frac{\mathrm{d}\boldsymbol{X}}{\mathrm{d}\tau} = \frac{\Delta P}{s}\boldsymbol{n}. \tag{4.4}$$

If the origin of the vertical coordinate $Y=0$ is placed at the maximum penetration depth of the foam front, then the solution domain extends from $Y=0$ to $Y=1$, and in dimensionless variables $\Delta P = Y$. Meanwhile s is updated according to $\mathrm{d}s/\mathrm{d}\tau = (\mathrm{d}\boldsymbol{X}/\mathrm{d}\tau).\boldsymbol{n}$. This now constitutes the (dimensionless) 2-D pressure-driven growth model for forward flow. In order to consider how the model might need to be modified in the presence of forward and reverse flow, we need first to examine analogous 1-D fractional flow models.

(b) Fractional-flow theory: Forward flow

Fractional-flow theory in 1-D is described by the Buckley-Leverett equation [59]

$$\partial(S_l\phi)/\partial t + \partial(qf_l)/\partial x = 0 \tag{4.5}$$

where S_l is liquid saturation, ϕ is porosity (assumed constant and uniform here), t is time, q is total flux of fluids (liquid and gas together; q is necessarily spatially uniform for incompressible fluids in 1-D), f_l is the fractional flow of liquid, and x is 1-D spatial coordinate. Physically equation (4.5) is nothing more than a conservation equation for liquid in the pores, and we consider it, in the first instance, in a forward flow mode with gas pushed into liquid. This can be solved by the method of characteristics [60]. As already alluded to, there will be a fan of characteristics in the x-t plane: S_l is constant along each characteristic. The slope of each characteristic line will be $(q/\phi)\mathrm{d}f_l/\mathrm{d}S_l$. Finding the solution therefore requires knowledge of the functional form of f_l vs S_l.

For the specific functional forms given in (3.1)–(3.3), Figure 3(a) plots f_l vs S_l in cases both with foam and without. In both cases, we see that f_l is small when S_l is small and f_l is close to unity when S_l is large. The main feature of interest in Figure 3(a) is that in the case of foam there is a sharp rise in f_l close to a certain S_l value, corresponding to the saturation $S_{l,*}$ above which foam films survive, but below which capillary suction causes foam films to collapse.

In 1-D fractional flow in forward flow mode, if gas is pushed into initially pure liquid (i.e. $S_l = f_l = 1$ initially) there must, at some location, be a boundary between a pure liquid region (downstream) and a region partly filled with gas (upstream). The Rankine-Hugoniot condition [60] tells us that this boundary propagates with a velocity $(q/\phi)\Delta f_l/\Delta S_l$ where Δf_l and ΔS_l are jumps in f_l and S_l at the boundary. The value of S_l immediately adjacent to this boundary must however be determined by matching with the speed of the corresponding characteristic which is $(q/\phi)f_l'(S_l)$. This then defines an equation for a so called contact discontinuity [60]

$$f_l'(S_{l,\rm fwd}) = (1-f_l(S_{l,\rm fwd}))/(1-S_{l,\rm fwd}). \tag{4.6}$$

The value $S_l = S_{l,\rm fwd}$ corresponding to this forward flow contact discontinuity is indicated on Figure 3(a). Comparing with equation (4.2) indicates that 2-D pressure-driven growth, at least in forward flow mode, is doing nothing more than capturing this contact discontinuity.

Returning to the 1-D fractional flow case, in the problem of interest we set up our coordinate system such that during forward flow $q<0$, so characteristics actually have negative slope. This

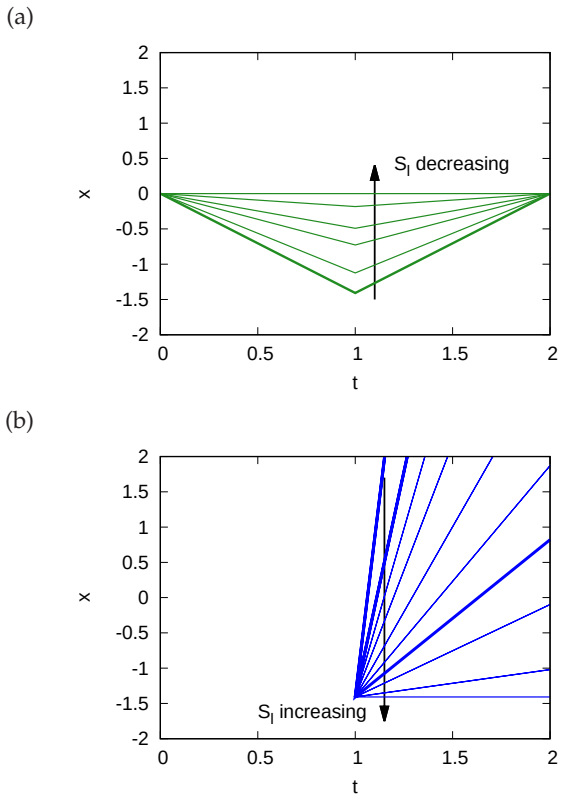

Figure 4. Characteristic fans during forward and reverse flow which occupy overlapping regions of the x-t plane. (a) Characteristic fan that appears during the forward flow phase corresponding to a set of low liquid saturations $0 \leq S_l \leq S_{l,\mathrm{fwd}} \equiv 0.3124$. The S_l values plotted (from bottom to top) are $S_l = S_{l,\mathrm{fwd}} \equiv 0.3124$, 0.31, 0.305, 0.3, 0.28 and 0, these values have been chosen to give a reasonable spacing between adjacent characteristics making the plot easier to view. All these characteristics are reflected after flow reversal at $t = 1$. (b) New characteristic fan that appears after flow reversal, originating from location $(x, t) = (x_{s,\mathrm{switch}}, t) = (-1.4083, 1)$ and corresponding to higher liquid saturations. The S_l values plotted are (top to bottom) $S_{l,\mathrm{infl}} \equiv 0.3520$ (shown as a thicker line), $S_{l,\mathrm{rev},0} \equiv 0.3672$ (again a thicker line), 0.3713 (the significance of this value is explained in Figure 6), 0.375, 0.38, 0.385, $S_{l,\mathrm{rev},\infty} \equiv 0.3904$ (thicker line), 0.4, 0.5 and 1. Again S_l values are chosen arbitrarily to give reasonable spacing between adjacent characteristics.

is as shown in Figure 2(b) (a sketch) and Figure 4(a) (an actual computation using data from equations (3.1)–(3.3)). The only S_l values admitted in the characteristic fan are those that have slopes of magnitude less than or equal to the slope of $S_{l,\mathrm{fwd}}$, i.e. only S_l values less than or equal to $S_{l,\mathrm{fwd}}$ are admitted. This is what Figure 2(b) and Figure 4(a) show. Note also (see Figure 3(c)) that the mobility M_{tot} at $S_{l,\mathrm{fwd}}$ is substantially lower than the mobility of pure gas at $S_l = 0$, albeit (for the present parameter values at least) still higher than M_{tot} of pure liquid at $S_l = 1$.

(c) Fractional-flow theory: Reverse flow

So far all we have done is review theories for conventional forward flow. Now we suppose that at a certain time t_r flow is reversed, so that q switches from negative to positive. We assume that the fractional flow curve (Figure 3(a)) curve is unchanged in forward and reverse flow. Even this is by no means certain however, since liquid invading a body of gas might cause a significant part of the gas to become trapped [61,62]. What we will discover however is that even assuming the same fractional flow curve, forward and reverse flow do not lead to the same mobility, since the

system can select different saturations (and hence different mobilities) according to whether flow is forward or reversed.

Assuming that the fractional flow curve remains unchanged as we have stated, it is clear that the slope of any given characteristic line is also reversed and this is what Figure 4(a) indicates: the characteristic fan that was produced originally is reflected and starts to close up on itself. For simplicity, we suppose that q has the same magnitude before and after the flow reversal, meaning the fan closes at the same rate as it originally opened. This simplifying assumption will not impact our ability to relate flow-reversed 1-D fractional flows to 2-D pressure-driven growth, since the information communicated between the different models concerns distances that fronts propagate, rather than propagation rates. Nevertheless finding the flow-reversed reflection of the original characteristic fan is not the full solution of the problem, as we will argue in what follows.

Before proceeding, it is convenient to make x dimensionless on the scale $t_r|q|/\phi$ and t dimensionless on the scale t_r. Note that these scales which are relevant for 1-D fractional flow differ from those which arise naturally 2-D pressure-driven growth in section (a), and we deliberately used distinct notation $\boldsymbol{X}$ and τ in 2-D to highlight the difference. The dimensionless equation for 1-D fractional flow (for compactness of notation, using the same symbols x and t as before) now becomes

$$\partial S_l/\partial t + \partial f_l/\partial x = 0 \tag{4.7}$$

with the flow reversal happening at dimensionless time $t = 1$. At this time, the boundary between pure liquid (which after flow reversal, is now considered upstream) and liquid and gas (downstream) is found at a dimensionless location $x = -f_l'(S_{l,\mathrm{fwd}})$.

In addition to the characteristic fan already mentioned above, a second characteristic fan appears now originates at $(x,t) = (-f_l'(S_{l,\mathrm{fwd}}), 1)$. This is sketched in Figure 2(b) and computed in Figure 4(b). The new fan has rather larger S_l values than before. Noting that f_l vs S_l exhibits an inflection point at some value $S_l = S_{l,\mathrm{infl}}$, the original fan corresponds to S_l values strictly less than $S_{l,\mathrm{infl}}$, whilst the new fan corresponds to S_l values greater than $S_{l,\mathrm{infl}}$. Note that, as Figure 2(b) and Figure 4 indicate, whereas S_l decreases moving upward through the original fan (the slope $f_l'(S_l)$ decreases in this direction), S_l actually increases moving downward through the new fan (again $f_l'(S_l)$ decreases in this direction).

It is clear from the regions plotted in Figure 4(a)–(b) that the two fans overlap. Any (x,t) location in the overlap region has in principle two distinct S_l values, one corresponding to each fan. However it is only usually possible to have two distinct S_l values at a single location if a shock is present. Thus as sketched in Figure 2(b) a shock divides the (x,t) plane into regions allocated to each fan, and only at the shock itself is S_l double valued.

If a shock is at a given location $x = x_s(t)$, then the two S_l values associated with it (denoted $S_{l,\mathrm{low}}$ and $S_{l,\mathrm{high}}$, indicating values respectively less than $S_{l,\mathrm{infl}}$ and greater than $S_{l,\mathrm{infl}}$) satisfy

$$f_l'(S_{l,\mathrm{low}}) = -x_s(t)/(2-t) \tag{4.8}$$

$$f_l'(S_{l,\mathrm{high}}) = (x_s(t) - x_{s,\mathrm{switch}})/(t-1) \tag{4.9}$$

where $x_{s,\mathrm{switch}}$ (i.e. the value of x_s at the instant of switching to flow reversal) satisfies $x_{s,\mathrm{switch}} \equiv -f_l'(S_{l,\mathrm{fwd}})$, i.e. it corresponds to the location that the original fan in the forward flow mode reached at dimensionless time $t = 1$. For our data $S_{l,\mathrm{fwd}} \approx 0.3124$ and $x_{s,\mathrm{switch}} \approx -1.4083$. Given t and $x_s(t)$, equations (4.8)–(4.9) are nonlinear equations to solve for $S_{l,\mathrm{low}}$ and $S_{l,\mathrm{high}}$. Equation (4.8) recognises that all characteristics on the reflection of the original forward flow fan focus in on $(x,t) = (0,2)$ (see Figure 4(a)), whereas equation (4.9) recognises that all characteristics on the new fan produced after $t = 1$ originate from $(x,t) = (x_{s,\mathrm{switch}}, 1)$ (see Figure 4(b)).

Once we know x_s, $S_{l,\mathrm{low}}$ and $S_{l,\mathrm{high}}$ and hence $f_{l,\mathrm{low}} \equiv f_l(S_{l,\mathrm{low}})$ and $f_{l,\mathrm{high}} \equiv f_l(S_{l,\mathrm{high}})$, we then also know how the shock trajectory evolves, according to a Rankine-Hugoniot condition [60]

$$\mathrm{d}x_s/\mathrm{d}t = \Delta f_l/\Delta S_l = (f_{l,\mathrm{high}} - f_{l,\mathrm{low}})/(S_{l,\mathrm{high}} - S_{l,\mathrm{low}}). \tag{4.10}$$

We can use equation (4.10) to update the shock location x_s between a time t and $t + \delta t$, and then for the new location, solve (4.8)–(4.9) for updated $S_{l,\mathrm{low}}$ and $S_{l,\mathrm{high}}$. An updated shock location

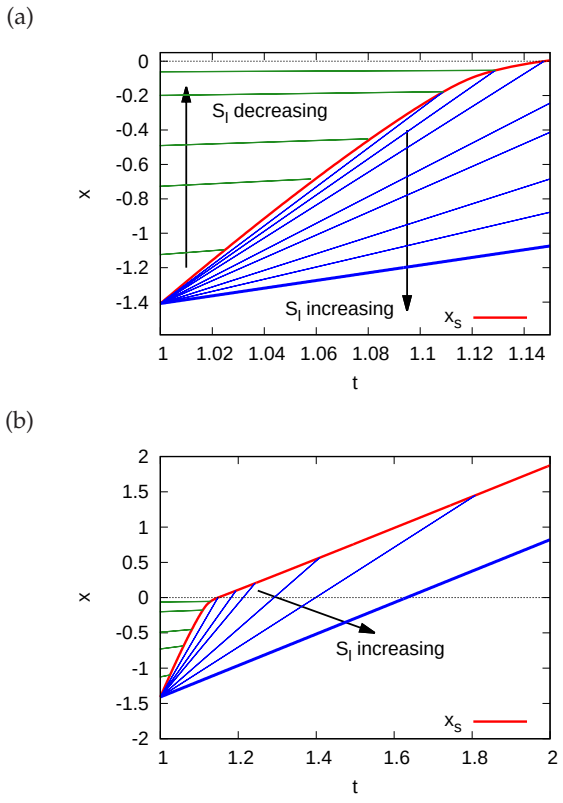

Figure 5. (a) Shock location x_s vs time t (shown as a curve) that separates two characteristic fans in the x-t plane (indicated by sets of straight lines). One fan with smaller S_l values is on the left (with S_l decreasing from bottom to top; S_l values plotted are 0.31, 0.305, 0.3, 0.2829, 0.1743, corresponding $M_{\rm tot}$ values are 3.3683, 3.8778, 4.2865, 5.0709, 6.8481). The other fan with larger S_l values is on the right, with S_l increasing from top to bottom; S_l values plotted are 0.369, 0.37, 0.3713, 0.374, 0.376, 0.38, 0.384 and $S_{l,{\rm rev},\infty} \equiv 0.3904$ (thicker line). Corresponding $M_{\rm tot}$ values are 0.1811, 0.1795, 0.1778, 0.1751, 0.1738, 0.1727, 0.1729 and 0.1751. Note that in the asymptotic limit as $t \to 1$ the shock starts out parallel to one of the characteristics in the fan on the right, specifically $S_l = S_{l,{\rm rev},0} \equiv 0.3767$. This is not plotted however as it only survives in the $t \to 1$ limit, and in that limit, it would be indistinguishable from the trajectory of the shock itself. (b) Zoomed out view of x_s vs t. When $x_s > 0$, only the characteristic fan on the right is relevant, and is plotted here with S_l values (from top to bottom) 0.3713, 0.374, 0.376, 0.38, 0.384 and $S_{l,{\rm rev},\infty} \equiv 0.3904$. Asymptotically as $t \to \infty$, the shock ends up parallel to this last mentioned characteristic.

for yet another time step can now be obtained using equation (4.10) and the process iterates. The result is plotted in Figure 5 (corresponding to a computation using a time step $\delta t = 0.001$): Figure 5(a) is a zoomed in view (for times just shortly after the instant of flow reversal), whereas Figure 5(b) is a zoomed out view (extending to rather longer times and hence larger x_s).

In order to obtain this solution, it is necessary to impose suitable initial conditions at $t = 1$. Not only (as already mentioned) is $x_s = x_{s,{\rm switch}}$ at this time, but also the value of $S_{l,{\rm low}}$ is necessarily $S_{l,{\rm fwd}}$ on the grounds that $x_{s,{\rm switch}}$ was determined by tracking a front with saturation $S_{l,{\rm fwd}}$ during the original forward flow mode. The initial value of $S_{l,{\rm high}}$ meanwhile is determined by recognising that in Figure 5(a), at $t = 1$ the trajectory of the shock in the x-t plane is initially parallel to a particular characteristic $S_{l,{\rm high}} = S_{l,{\rm rev},0}$ with

$$f_l'(S_{l,{\rm rev},0}) = (f_l(S_{l,{\rm rev},0}) - f_l(S_{l,{\rm fwd}}))/(S_{l,{\rm rev},0} - S_{l,{\rm fwd}}), \tag{4.11}$$

this value $S_l = S_{l,\mathrm{rev},0}$ also being indicated on the f_l vs S_l plot in Figure 3(a). We find $S_{l,\mathrm{rev},0} \approx 0.3672$. Note also in Figure 3(c) that the mobility M_{tot} at $S_{l,\mathrm{rev},0}$ is substantially lower than at $S_{l,\mathrm{fwd}}$, and lower even than the M_{tot} value for pure liquid (which is unity by definition).

The implication of equation (4.11) is that the "shock" strictly speaking starts out asymptotically as a contact discontinuity (in the x-t plane characteristics enter it from one side only, being parallel to it on the other side), and only evolves with time to become a true shock (characteristics enter it on both sides). What this means geometrically in Figure 5(a), is that if we select any characteristic in the left hand fan and follow it in the direction of increasing t, it is never parallel to the shock, and therefore must enter, i.e. intersect with, the shock. Meanwhile for the right hand fan, in the limit at $t \to 1$, the shock starts off parallel to one of the characteristics, which (moving in the direction of increasing t) initially prevents that characteristic and the shock from intersecting.

As the shock moves upwards over time, the liquid saturation on its "low" S_l side falls. This is indicated in Figure 5(a) (see the characteristics to the left of the shock) and is also shown directly in Figure 6(a). As $S_{l,\mathrm{low}}$ falls, the difference $\Delta S_l = S_{l,\mathrm{high}} - S_{l,\mathrm{low}}$ grows, for a relatively modest change in $\Delta f_l = f_{l,\mathrm{high}} - f_{l,\mathrm{low}}$ as Figure 7(a) makes clear. Via (4.10), a consequence is that $\mathrm{d}x_s/\mathrm{d}t$ falls, meaning the shock is necessarily a curve in the x-t plane (as Figure 5(a) shows), unlike the characteristics themselves which are straight lines. Once the shock trajectory starts to reorient over time, we can follow characteristics in the right hand fan in Figure 5(a) in the direction of increasing t and now see them entering, i.e. intersecting with, the shock. Moreover the intersection corresponds to characteristics with increasingly large $S_{l,\mathrm{high}}$ values as time proceeds. This is clear from Figure 5(a)–(b) and also from Figure 7(a)–(b). Values of $S_{l,\mathrm{high}}$ are plotted vs t in Figure 6(b). Note that (see Figure 5 and 7) the speed of the shock $\mathrm{d}x_s/\mathrm{d}t$ exceeds the slope of the characteristic $f_l'(S_{l,\mathrm{low}})$ on the "low" saturation side, but is less than the slope of the characteristic $f_l'(S_{l,\mathrm{high}})$ on the "high" saturation side: in Figure 5 therefore, characteristics do indeed enter the shock from sides. Comparisons between the shock speed and the speeds associated with characteristics either side of it are plotted vs time on Figure 8(a).

(d) Reverse flows at longer times and/or larger reverse displacements

Figure 5 indicates that, in our 1-D model, at a certain time the shock crosses over the location $x = 0$, meaning that, during the reverse flow phase, the shock has now covered the exact same distance spanned by the fan during the original forward flow phase. In the context of a 2-D pressure-driven growth model, certain points on a front would likely stop before they backtracked through a distance equivalent to the distance covered during an initial forward flow phase: in Figure 2(a) a point which, at the instant of flow reversal, was immediately below point B would be an example. It would only ever backtrack to the neutral depth, indicated in Figure 2(a) by a bold dashed line which happens to pass through point B. However other points can backtrack further than they moved forward initially. Point C is an example. It followed a relatively short curved path to reach its location in Figure 2(a) (close what was originally the bottom of the foam front) but upon flow reversal can backtrack all the way to the neutral depth (the bold dashed line). This is a 2-D picture of course in which depth influences net driving pressure difference, and hence the flux which that pressure difference generates. For the present however we focus on a 1-D model, in which the flux is specified, undergoing a change in sign but not in magnitude upon flow reversal.

In the 1-D system, how far the shock backtracks then depends upon how long the reverse flow phase persists: the shock x_s will always manage to cross over $x = 0$ provided the reverse flow phase persists for long enough. Since the shock that appears after $t = 1$ has a speed that is rather faster than the original forward flow during $t \leq 1$, this cross over happens well before $t = 2$ as Figure 5(a) shows, i.e. it happens well before the original "forward flow" fan focuses in completely upon itself. In our data $x_s = 0$ at time $t \approx 1.1476$. We denote this cross-over time t_{cross}.

The time t_{cross} signals a change in the structure of the solution for how S_l varies with x. This change can be inferred by tracing through the characteristic pattern in Figure 5 varying spatial coordinate x at any fixed time t: results of doing this at various times are plotted in Figure 9.

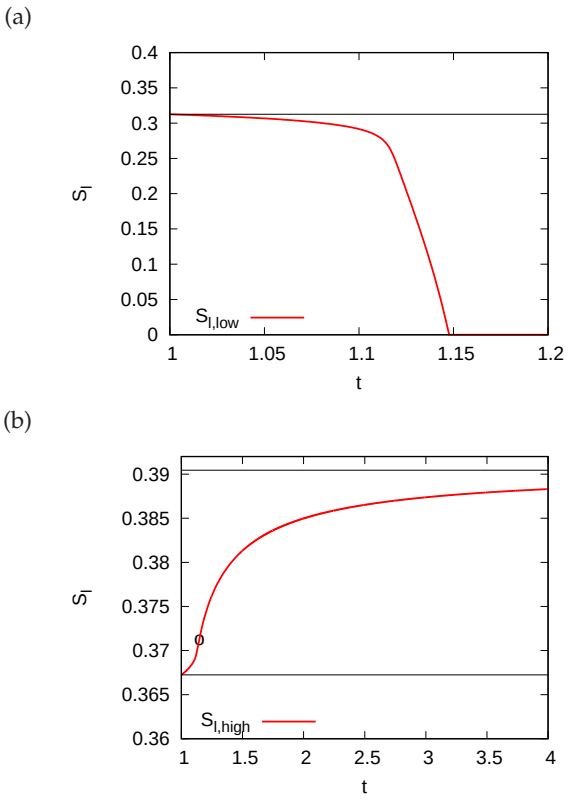

Figure 6. Liquid saturations either side of the shock vs time. (a) $S_{l,\mathrm{low}}$ vs t. The horizontal line denotes the value $S_{l,\mathrm{fwd}}$. (b) $S_{l,\mathrm{high}}$ vs t. The horizontal lines denote the values $S_{l,\mathrm{rev},0}$ and $S_{l,\mathrm{rev},\infty}$. The circle indicates the time $t_{\mathrm{cross}} \approx 1.1476$ at which the shock x_s crosses $x = 0$, which is also the time at which $S_{l,\mathrm{low}}$ falls to zero. The corresponding $S_{l,\mathrm{high}}$ value at this particular time is $S_{l,\mathrm{high}} \approx 0.3713$.

During the reverse flow at some time t greater than unity but prior to time t_{cross}, sufficiently far upstream i.e. for $x \leq x_{s,\mathrm{switch}}$ we have pure liquid (or more generally a maximum liquid saturation beyond which gas is irreducible), whereas sufficiently far downstream for $x \geq 0$ we have pure gas (or more generally irreducible liquid). As we move from $x = x_{s,\mathrm{switch}}$ to $x = 0$, the value of S_l (see Figure 9) falls continuously through the fan from $S_l = 1$ down to $S_l = S_{l,\mathrm{high}}$, then it jumps immediately to $S_{l,\mathrm{low}}$ at the shock $x = x_s$, and subsequently falls continuously through the fan to $S_l = 0$. This rather complex S_l vs x profile therefore follows from the complex double fan structure that is developed around the shock.

After time t_{cross} however, on the "low" saturation side of the shock, $S_{l,\mathrm{low}}$ has already fallen to zero (or more generally to an irreducible S_l). The S_l vs x profile in Figure 9 now changes, with S_l falling to zero immediately downstream of the shock. The shock now invades an entirely gas filled region, rather than invading a mixed gas-liquid fan that developed during the original forward flow phase. Only a single fan remains relevant now (i.e. the fan on the "high" saturation side of the shock), with S_l falling continuously from $S_l = 1$ at $x = x_{s,\mathrm{switch}}$ to $S_{l,\mathrm{high}}$ at $x = x_s$. Since the shock velocity $\Delta f_l / \Delta S_l$ (which reduces to $f_{l,\mathrm{high}}/S_{l,\mathrm{high}}$ under the present circumstances), remains less than the slope of the characteristic $f_l'(S_{l,\mathrm{high}})$ (this can be seen in Figure 5(b)) the shock continues to evolve towards higher and higher values of $S_{l,\mathrm{high}}$. However increasing $S_{l,\mathrm{high}}$ (with $S_{l,\mathrm{low}}$ fixed at zero), tends to increase the speed of the shock, as is seen in Figure 8(b): the shock decelerates between $t = 1$ and $t = t_{\mathrm{cross}}$, but accelerates again after t_{cross}.

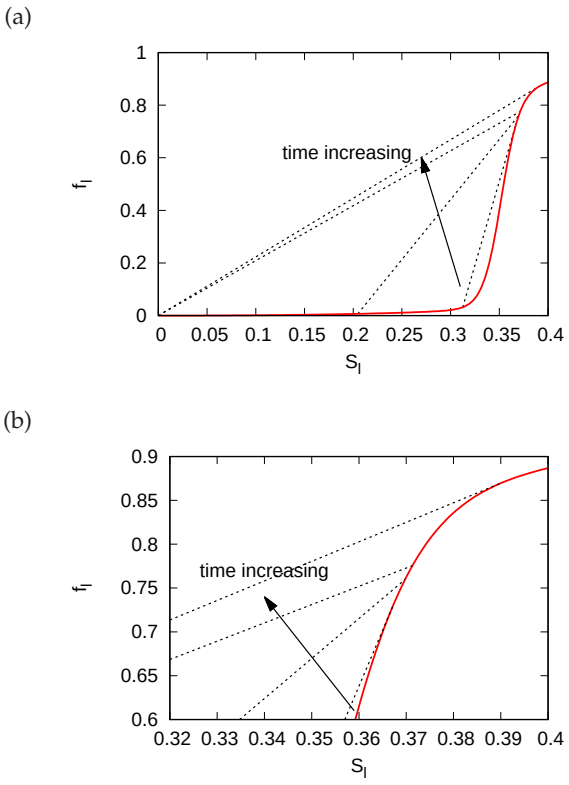

Figure 7. (a) Fractional flow curve f_l vs S_l with dashed lines drawn indicating (at various times) the shock joining $(S_{l,\mathrm{low}}, f(S_{l,\mathrm{low}}))$ to $(S_{l,\mathrm{high}}, f(S_{l,\mathrm{high}}))$. The specific times corresponding to the dashed lines are $t = 1$ (the instant of flow reversal), $t = 1.125$, $t = 1.1476$ (the instant t_{cross} at which $x_s = 0$ and $S_{l,\mathrm{low}}$ falls to zero), and $t \to \infty$. (b) Zoomed view, showing in particular how $S_{l,\mathrm{high}}$ grows over time. Note that the high S_l end of the shock (dashed line) is only tangent to the fractional flow curve when $t = 1$ and when $t \to \infty$, but not for intermediate times.

There is however a limit to how much the shock can accelerate. The system asymptotes to a S_l value that we denote $S_{l,\mathrm{rev},\infty}$ at which the shock speed matches the speed of a characteristic

$$f_l'(S_{l,\mathrm{rev},\infty}) = f_l(S_{l,\mathrm{rev},\infty})/S_{l,\mathrm{rev},\infty}. \tag{4.12}$$

The value of $S_{l,\mathrm{rev},\infty}$ is indicated on Figure 3(a). As the shock asymptotes to this particular characteristic, at long times the shock evolves towards a contact discontinuity again, albeit a different contact discontinuity from what was seen at the instant of flow reversal. Note that this contact discontinuity with $S_l = S_{l,\mathrm{rev},\infty}$ corresponds to what we would have in a situation in which the front underwent a reverse flow (i.e. liquid pushed into gas) without any initial forward flow phase. At sufficiently long times therefore, the reverse flow has proceeded for long enough that the initial forward flow phase no longer has a bearing on the solution.

(e) Pressure required to drive fractional flow

So far our analysis of the 1-D fractional flow model has considered a specified flux of fluids (liquid plus gas) denoted q in dimensional variables, but has not considered anything about the pressure difference needed to drive though fluids along. This pressure difference (reverting to dimensional variables) is given by $\Delta p = \int q/(k\mathcal{M}_{\mathrm{tot}})\,\mathrm{d}x \equiv \int q\mu_l/(kM_{\mathrm{tot}})\,\mathrm{d}x$ where the integral needs to proceed from an upstream location to a downstream one (we leave the exact integration

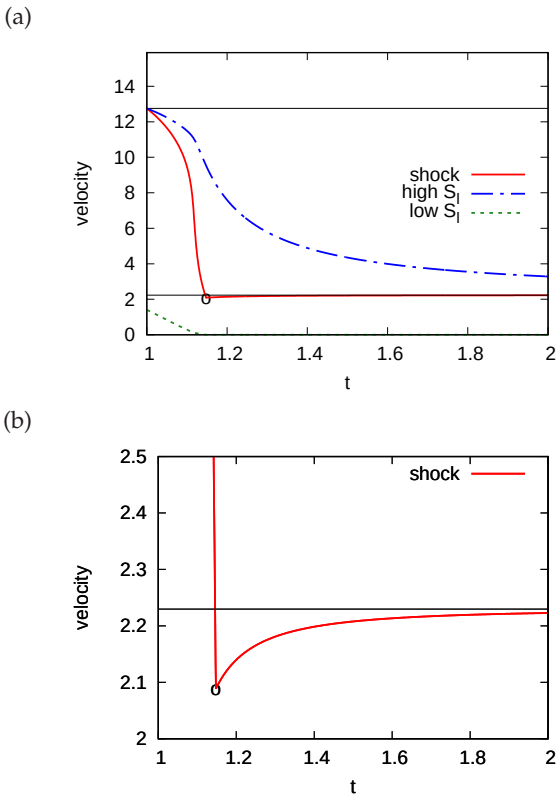

Figure 8. (a) Speed of the shock compared with speed of characteristics on both the high S_l side of the shock and the low S_l side. The horizontal lines indicate the initial and final speeds of the shock (which coincide with the speeds of the characteristics respectively at $S_{l,\mathrm{rev},0}$ and $S_{l,\mathrm{rev},\infty}$). The circle indicates the time t_{cross} at which the shock x_s crosses $x_s = 0$, which is also the time at which $S_{l,\mathrm{low}}$ falls to zero. (b) Zoomed view showing just the shock velocity.

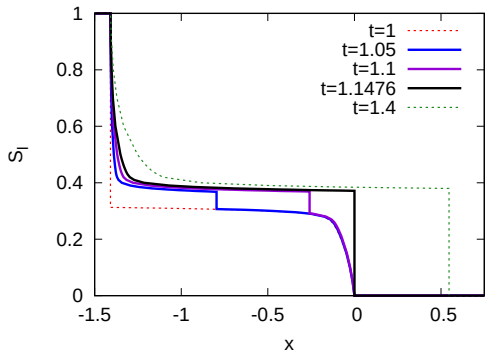

Figure 9. Plot of S_l vs x at various times, $t = 1$ (the instant of flow reversal), $t = 1.05$, $t = 1.1$, $t = 1.1476$ (the time t_{cross} at which the shock location x_s crosses zero) and $t = 1.4$.

limits unspecified for the moment). Remembering that distances can be non-dimensionalised on a scale $t_r|q|/\phi$, and supposing we define $\Delta\mathcal{P}$ via $\Delta p = \mu_l q^2 t_r/(k\phi)\Delta\mathcal{P}$, a dimensionless analogue is obtained (for compactness of notation, using x now to denote dimensionless coordinate)

$$\Delta\mathcal{P} = \int \mathrm{d}x/M_{\mathrm{tot}}. \tag{4.13}$$

Here M_{tot} is a known function of liquid saturation S_l (see Figure 3(b)), but (at any dimensionless time t), S_l is also a known function of dimensionless coordinate x.

For the data used here, values of M_{tot} vs S_l are plotted in Figure 3(b)–(c) and have already been discussed back in section 3(d). Recall that pure gas is ten times more mobile here than pure liquid, so that as S_l increases, M_{tot} tends to decrease. Moreover, at a certain S_l value, recall that M_{tot} exhibits a sharp decrease due to the presence of foam. The total mobility for any higher S_l values is then almost entirely accounted for by the liquid relatively mobility alone (as is seen in Figure 3(c)), but this can still be rather less than the mobility of pure liquid. Mixtures of gas and liquid can thereby have substantially lower mobility than either pure liquid or pure gas.

If gas-liquid mixtures found within characteristic fans thereby make the dominant contribution to the pressure drop, it is possible to change the integration variable from x to S_l leading to

$$\Delta\mathcal{P} \approx \int_0^{S_{l,\mathrm{low}}} \frac{1}{M_{\mathrm{tot}}} \left|\frac{\mathrm{d}x}{\mathrm{d}S_l}\right| \mathrm{d}S_l + \int_{S_{l,\mathrm{high}}}^1 \frac{1}{M_{\mathrm{tot}}} \left|\frac{\mathrm{d}x}{\mathrm{d}S_l}\right| \mathrm{d}S_l. \tag{4.14}$$

The integral is divided into two parts, one for each fan (assuming time t is less than t_{cross}, otherwise just a single fan, i.e. the "high" S_l fan, is relevant). In the low S_l fan, $x = -f_l'(S_l)(2-t)$ whereas in the high S_l fan, $x = f_l'(S_l)(t-1) + x_{s,\mathrm{switch}}$. Equation (4.14) therefore becomes

$$\Delta\mathcal{P} \approx \int_0^{S_{l,\mathrm{low}}} \frac{1}{M_{\mathrm{tot}}(S_l)} |f_l''(S_l)|(2-t)\,\mathrm{d}S_l + \int_{S_{l,\mathrm{high}}}^1 \frac{1}{M_{\mathrm{tot}}(S_l)} \left|f_l''(S_l)\right| (t-1)\,\mathrm{d}S_l. \tag{4.15}$$

The exact values of the integrals in the above depend on the functional forms of M_{tot} and f_l''. These integrals are quite complex, since at first sight S_l values with the smallest M_{tot} should contribute the most, but these also tend to have smallest f_l'' (close to the inflection point of f_l). Close to the inflection point, moderate changes in S_l produce only very small changes in x implying a limited contribution to pressure drop.

Despite this complexity, what is clear however is that early on, i.e. immediately after the instant of flow reversal $t = 1$, the pressure drop is dominated by the first integral (arising from the "low" S_l fan) since the second integral (from the "high" S_l fan) vanishes. As time proceeds however, the balance necessary shifts from the first to the second integral, partly because of the factor $2-t$ decreasing whilst $t-1$ increases, but also because of the integration limit $S_{l,\mathrm{low}}$ in the first integral falling towards zero. By the time $t = t_{\mathrm{cross}}$ at which x_s crosses over $x = 0$, the value of $S_{l,\mathrm{low}}$ has fallen to zero, and so only the second integral survives.

One way of approximating these complex integrals, is to revert to equation (4.13), but integrating now in two sections from $x = x_s$ to $x = 0$ (the low S_l fan) and from $x = x_{s,\mathrm{switch}}$ to $x = x_s$ (the high S_l fan). Hence

$$\Delta\mathcal{P} \approx \int_{x_s}^0 \frac{1}{M_{\mathrm{tot}}(S_l(x))}\,\mathrm{d}x + \int_{x_{s,\mathrm{switch}}}^{x_s} \frac{1}{M_{\mathrm{tot}}(S_l(x))}\,\mathrm{d}x. \tag{4.16}$$

On each fan the lowest M_{tot} values arise from the S_l values closest to the shock (i.e. from the values $S_{l,\mathrm{low}}$ and $S_{l,\mathrm{high}}$). Given that these are the lowest values of mobility M_{tot}, they make the largest contribution to each integral in equation (4.16). We now suppose that M_{tot} stays close to these lowest mobility values over a fraction $\varepsilon \ll 1$ of each integration domain (the shaded regions in Figure 2(b) represent these portions of the domain schematically), and we suppose that M_{tot} is much larger in other parts of the integration domain. Hence the integrals can be assumed to

	$R_f = 185$	$R_f = 1850$	$R_f = 18500$
$S_{l,\mathrm{fwd}}$	0.3124	0.2911	0.2700
$f_l(S_{l,\mathrm{fwd}})$	0.0316	0.0278	0.0245
$M_{\mathrm{tot,fwd}}$	*3.0861*	*3.0473*	*2.9692*
$S_{l,\mathrm{infl}}$	0.3520	0.3317	0.3107
$M_{\mathrm{tot,infl}}$	0.2786	0.2199	0.1906
$S_{l,\mathrm{rev},0}$	0.3672	0.3468	0.3258
$f_l(S_{l,\mathrm{rev},0})$	0.7302	0.8253	0.8382
$M_{\mathrm{tot,rev},0}$	0.1846	0.1457	0.1266
$S_{l,\mathrm{min\ mob}}$	0.3811	0.3586	0.3368
$M_{\mathrm{tot,min}}$	0.1727	0.1377	0.1202
$S_{l,\mathrm{rev},\infty}$	0.3904	0.3657	0.3436
$f_l(S_{l,\mathrm{rev},\infty})$	0.8705	0.9604	0.9714
$M_{\mathrm{tot,rev},\infty}$	0.1751	0.1392	0.1215

Table 2. Key liquid saturations ($S_{l,\mathrm{fwd}}$, $S_{l,\mathrm{infl}}$, $S_{l,\mathrm{rev},0}$, $S_{l,\mathrm{min\ mob}}$, $S_{l,\mathrm{rev},\infty}$) and associated total mobilities ($M_{\mathrm{tot,fwd}}$, $M_{\mathrm{tot,infl}}$, $M_{\mathrm{tot,rev},0}$, $M_{\mathrm{tot,min}}$, $M_{\mathrm{tot,rev},\infty}$) for different values of the foam mobility reduction factor R_f. We consider here not only the base case value $R_f = 185$, but also higher values $R_f = 1850$ and $R_f = 18500$ (discussed further in supplementary material). Any total mobility values shown in italics actually exceed the mobility of pure liquid (normalised to unity here). It is only for total mobilities (not in italics) that are substantially smaller than unity that it is reasonable to suppose the the bulk of the dissipative pressure drop occurs close to the foam front. A number of f_l values are also reported, specifically for $S_{l,\mathrm{fwd}}$, $S_{l,\mathrm{rev},0}$ and $S_{l,\mathrm{rev},\infty}$, these f_l values being needed to determine shock speeds via the Rankine-Hugoniot condition.

evaluate to

$$\Delta\mathcal{P} \approx \frac{|x_s|\varepsilon}{M_{\mathrm{tot}}(S_{l,\mathrm{low}})} + \frac{|x_s - x_{s,\mathrm{switch}}|\varepsilon}{M_{\mathrm{tot}}(S_{l,\mathrm{high}})} \tag{4.17}$$

where the first term on the right hand side is only relevant when $x_s < 0$ (otherwise the term is discarded, which follows because, when $x_s > 0$ there is no longer a fan on the "low" S_l side of the shock, only on the "high" S_l side; see Figure 5(b)). Provided $x_s < 0$, so that both terms on the right hand side are included, we *assume* here (for simplicity) that the same value ε is applicable on both sides of the shock, although this could be generalised to having different ε values on the "low" and "high" side.

We now approximate further by assuming that at all times, $M_{\mathrm{tot}}(S_{l,\mathrm{low}})$ can be estimated by $M_{\mathrm{tot}}(S_{l,\mathrm{fwd}})$ (hereafter denoted $M_{\mathrm{tot,fwd}}$), and $M_{\mathrm{tot}}(S_{l,\mathrm{high}})$ can be estimated by $M_{\mathrm{tot}}(S_{l,\mathrm{rev},\infty})$ (hereafter denoted $M_{\mathrm{tot,rev},\infty}$). The latter approximation is a relatively good one, since M_{tot} changes relatively little as $S_{l,\mathrm{high}}$ evolves from $S_{l,\mathrm{rev},0}$ to $S_{l,\mathrm{rev},\infty}$ (see Table 2 and also Figure 3(c)). This follows because both $S_{l,\mathrm{rev},0}$ and $S_{l,\mathrm{rev},\infty}$ tend to be close to a value that we denote $S_{l,\mathrm{min\ mob}}$ at which mobility M_{tot} reaches an overall minimum $M_{\mathrm{tot,min}}$. The former approximation is less robust, although significant falls in $S_{l,\mathrm{low}}$ below $S_{l,\mathrm{fwd}}$ leading in turn to significant rises in M_{tot} (see Figure 3(c)) only tend to happen for (dimensionless) times bigger than about 1.1 (see Figure 6(a)) by which time $|x_s|$ has shrunk to around 20% of the original value it had at unit time (see Figure 5(a)). This makes the first term on the right hand side of equation (4.17) relatively unimportant anyway.

If we rearrange equation (4.17) and convert it back in terms of dimensional pressure and dimensional coordinate, we deduce

$$q = \frac{k\,\Delta p}{\mu_l}\left(\frac{|x_s|\varepsilon}{M_{\mathrm{tot,fwd}}} + \frac{|x_s - x_{s,\mathrm{switch}}|\varepsilon}{M_{\mathrm{tot,rev},\infty}}\right)^{-1} \tag{4.18}$$

where again the first term in parentheses on the right hand side is only relevant to situations in which $x_s < 0$, otherwise the term is discarded.

(f) Implications of the pressure drop vs flux relation

Equation (4.18) allows us to relate the total fluid flux q to an imposed pressure difference Δp for a 1-D forward-and-reverse fractional flow: the consequences of this equation are now explored. Immediately after flow switches from forward to reverse flow mode, $|x_s - x_{s,\mathrm{switch}}| \gg |x_s|$, so the first term on the right hand side of (4.18) dominates the second: the bulk of the pressure drop occurs across the reflection of the original characteristic fan that was developed during forward flow. As time proceeds however $|x_s|$ decreases whilst $|x_s - x_{s,\mathrm{switch}}|$ grows, so the balance within (4.18) shifts from the first to the second term. Moreover this shift can actually happen quite quickly even before x_s has displaced very far from $x_{s,\mathrm{switch}}$, since $M_{\mathrm{tot,rev},\infty}$ tends to be significantly smaller than $M_{\mathrm{tot,fwd}}$, as Figure 3(c) and Table 2 show.

In fact for the system we are currently considering it turns out that $M_{\mathrm{tot,fwd}}$ is actually larger than unity (see Table 2). This means that the total mobility associated with the forward flow characteristic fan that develops when gas propagates into liquid (i.e. a fan with relatively high saturations of gas, but relatively low saturations of liquid up to $S_{l,\mathrm{fwd}}$) is actually *greater* than the mobility of pure liquid (since pure liquid has $M_{\mathrm{tot}} \equiv 1$ by definition). Saturations which produce much lower mobilities, whilst they exist in principle within Figure 3(c), are not being selected in forward flow mode, at least not in forward flow mode with our current parameter set.

This has a number of implications. It means for instance that, for our parameter set, the pressure drop across parts of the flow domain that are entirely filled with liquid cannot necessarily be neglected, despite one of the assumptions used to justify pressure-driven growth [40] having been that the mobility of mixed gas-liquid flows (within characteristic fans) is much lower than the mobility of pure liquid or pure gas flows outside fans. Nevertheless under circumstances with $M_{\mathrm{tot,fwd}} > 1$, equation (4.18) can still be considered applicable to determine total fluid fluxes q but Δp now needs to be interpreted to mean pressure drop applied across the characteristic fan region, which will generally be less than the pressure drop applied across the entire flow field.

Moreover in the situation of interest here, any issues with applicability of equation (4.18) gradually resolve themselves over time. During forward and reverse flow, we know that a second characteristic fan is produced upon the instant of flow reversal. This fan (corresponding to pushing liquid into a gas-liquid mixture) has relatively high liquid saturations and the mobility $M_{\mathrm{tot,rev},\infty}$ that we associate with it really does satisfy $M_{\mathrm{tot,rev},\infty} \ll 1$ (see Table 2). It is then reasonable to suppose that the bulk of any imposed pressure drop really does occur across that particular characteristic fan. Whereas $S_{l,\mathrm{fwd}}$ corresponds a point at which M_{tot} in the presence of foam is still relatively high, but is just beginning to fall below M_{tot} in the absence of foam, by way of contrast $S_{l,\mathrm{rev},\infty}$ gives a M_{tot} value in the presence of foam that is very much smaller and actually close to a global minimum. Ironically then, despite the 2-D pressure-driven growth model having been developed originally for a forward flow situation, the underlying 1-D fractional-flow theory implies via equation (4.18) that the assumption underlying pressure-driven growth (i.e. the assumption that $M_{\mathrm{tot}} \ll 1$ for mixed liquid and gas flow) is actually more robust in a forward and reverse flow situation such as we consider here. The way to use equation (4.18) to generalise pressure-driven growth to a forward and reverse flow mode is discussed next.

(g) Forward and reverse flow: Pressure-driven growth

In a 2-D pressure-driven growth scenario, consider a situation in which an initial injection pressure P_{inj} suddenly reduced to a multiple $(1-\chi)$ of its original value for some $\chi < 1$. If the injection pressure and hydrostatic pressure originally came into balance at a unit dimensionless depth below the top of the foam front, they will now come into balance at a depth of $(1-\chi)$ units, i.e. at a location χ units higher up than before. If we then set, as before, the zero of our coordinate vertical system at the original "neutral" depth at which injection pressure and hydrostatic pressure originally balanced, the new "neutral" Y location shifts to $Y_{\mathrm{neut}} = \chi$: this is indicated schematically by the bold dashed line in Figure 2(a) which has shifted upwards relative to what was originally the bottom of the front. For any points satisfying $Y > Y_{\mathrm{neut}}$,

equation (4.4) continues to apply, just with a new formula for (dimensionless) net driving pressure. In dimensionless form we have $\mathrm{d}\boldsymbol{X}/\mathrm{d}\tau = ((Y - Y_{\mathrm{neut}})/s)\,\boldsymbol{n}$.

The situation described above is a minor modification of conventional pressure-driven growth, so we do not consider it any further. Instead points satisfying $Y < Y_{\mathrm{neut}}$ are of interest here. For such points it is convenient upon flow reversal to switch the direction of the front normal (so as to align it with the direction of the arrows shown in Figure 2(a)), ensuring it continues to point along the direction in which net pressure decreases, which is now from liquid towards gas. For any given point with $Y < Y_{\mathrm{neut}}$, we define a distance s_{switch} that it displaced up to the point at which flow reversal occurred, and we also define a distance s_{since} that it has backtracked since flow reversal.

We are now in a position to generalize equation (4.18) to a situation of 2-D pressure-driven growth recognising that s_{switch} can be identified with $|x_{s,\mathrm{switch}}|$ in that equation, whereas s_{since} can be identified with $|x_s - x_{s,\mathrm{switch}}|$. We therefore deduce (in dimensional variables)

$$\boldsymbol{q} \equiv q\,\boldsymbol{n} = \frac{k\,\Delta P}{\mu_l}\left(\frac{|s_{\mathrm{switch}} - s_{\mathrm{since}}|\varepsilon}{M_{\mathrm{tot,fwd}}} + \frac{s_{\mathrm{since}}\varepsilon}{M_{\mathrm{tot,rev},\infty}}\right)^{-1}\boldsymbol{n}. \tag{4.19}$$

This applies to points satisfying $s_{\mathrm{since}} < s_{\mathrm{switch}}$, i.e. that have backtracked less than they moved in the original forward flow phase. During pressure-driven growth, some points satisfy this constraint at all times, e.g. in Figure 2(a) points that start backtracking just slightly below point B will reach the neutral depth, indicated by the horizontal bold dashed line in Figure 2 (at which point s_{since} stops evolving), long before s_{since} (the distance backtracked) is anywhere near s_{switch} (the distance moved forward originally). Other points however (point C in Figure 2(a) for instance) potentially backtrack further than they moved forward initially. Analogously with what we saw for equation (4.18), once $s_{\mathrm{since}} > s_{\mathrm{switch}}$, the first term in the parenthesis on the right hand side of equation (4.19) is discarded, and only the second term survives.

Equation (4.19) gives a total fluid flux, but not yet the velocity at which a pressure-driven growth front propagates. To establish this we draw an analogy with equation (4.2) to deduce (again in dimensional variables)

$$\frac{\mathrm{d}\boldsymbol{X}}{\mathrm{d}\tau} = \frac{q}{\phi}\frac{\Delta f_l}{\Delta S_l}\boldsymbol{n}. \tag{4.20}$$

This recognizes that what we are now tracking is a shock with speed $(q/\phi)\Delta f_l/\Delta S_l$ with Δf_l and ΔS_l being jumps in fractional flow and in liquid saturation across the shock. This therefore generalises equation (4.2) (forward flow mode) in which a contact discontinuity propagated with speed $(q/\phi)(1 - f_l)/(1 - S_l)$.

Combining equation (4.19) and (4.20) gives

$$\frac{\mathrm{d}\boldsymbol{X}}{\mathrm{d}\tau} = \frac{k\,\Delta P}{\phi\mu_l}\left(\frac{|s_{\mathrm{switch}} - s_{\mathrm{since}}|\varepsilon}{M_{\mathrm{tot,fwd}}} + \frac{s_{\mathrm{since}}\varepsilon}{M_{\mathrm{tot,rev},\infty}}\right)^{-1}\frac{\Delta f_l}{\Delta S_l}\boldsymbol{n}. \tag{4.21}$$

It is clear from the results of Figure 6–7 that Δf_l and ΔS_l are functions of time since flow reversal. However the data of Figure 5 indicate that to a reasonable approximation

$$\Delta f_l/\Delta S_l \approx (f_{l,\mathrm{rev},0} - f_{l,\mathrm{fwd}})/(S_{l,\mathrm{rev},0} - S_{l,\mathrm{fwd}}) \tag{4.22}$$

provided $x_s < 0$ (i.e. provided $s_{\mathrm{since}} < s_{\mathrm{switch}}$), whereas

$$\Delta f_l/\Delta S_l \approx f_{l,\mathrm{rev},\infty}/S_{l,\mathrm{rev},\infty} \tag{4.23}$$

if $x_s > 0$ (i.e. $s_{\mathrm{since}} > s_{\mathrm{switch}}$).

In dimensionless form (using the same dimensionless scales as used back in section (a), and retaining the same symbols $\boldsymbol{X}$ and τ for compactness of notation) equation (4.21) now reduces to

$$\frac{\mathrm{d}\boldsymbol{X}}{\mathrm{d}\tau} = |Y - Y_{\mathrm{neut}}|\left(|s_{\mathrm{switch}} - s_{\mathrm{since}}| + s_{\mathrm{since}}\frac{M_{\mathrm{tot,fwd}}}{M_{\mathrm{tot,rev},\infty}}\right)^{-1}\frac{(f_{l,\mathrm{rev},0} - f_{l,\mathrm{fwd}})}{(S_{l,\mathrm{rev},0} - S_{l,\mathrm{fwd}})}\frac{(1 - S_{l,\mathrm{fwd}})}{(1 - f_{l,\mathrm{fwd}})}\boldsymbol{n} \tag{4.24}$$

which applies for $Y < Y_{\rm neut}$ and $s_{\rm since} < s_{\rm switch}$. Here $|Y - Y_{\rm neut}|$ is the dimensionless analogue of ΔP, while equation (4.22) has been used as an approximation for $\Delta f_l/\Delta S_l$. Meanwhile for a situation in which $s_{\rm since} > s_{\rm switch}$ (still with $Y < Y_{\rm neut}$), we have instead

$$\frac{{\rm d}\boldsymbol{X}}{{\rm d}\tau} = |Y - Y_{\rm neut}| \frac{M_{\rm tot,rev,\infty}}{M_{\rm tot,fwd}\, s_{\rm since}} \frac{f_{l,{\rm rev},\infty}}{S_{l,{\rm rev},\infty}} \frac{(1 - S_{l,{\rm fwd}})}{(1 - f_{l,{\rm fwd}})} \boldsymbol{n}. \tag{4.25}$$

Here we only need to consider a low mobility fan growing proportionally to $s_{\rm since}$ located behind the shock, but without any fan surviving ahead of it, which is why terms in $|s_{\rm switch} - s_{\rm since}|$ have been discarded. Also equation (4.23) has been used in place of (4.22). The value of $s_{\rm switch}$ (dimensionless distance travelled up to the instant of flow reversal) is inherited from the original forward flow propagation of the front, whilst the value of $s_{\rm since}$ (dimensionless distance travelled since flow reversal) satisfies

$$ {\rm d}s_{\rm since}/{\rm d}\tau = ({\rm d}\boldsymbol{X}/{\rm d}\tau).\boldsymbol{n} \tag{4.26}$$

with $s_{\rm since} = 0$ at the instant of flow reversal.

Equations (4.24)–(4.26) are the key results in this paper, providing a well-defined way to generalise pressure-driven growth to the case of flow reversal. We make the following observations. As already noted in section (f), via Table 2, the ratio $M_{\rm tot,fwd}/M_{\rm tot,rev,\infty}$ tends to be considerably larger than unity, meaning that within the parentheses in equation (4.24), the second term can dominate the first term even for $s_{\rm since}$ values considerably smaller than $|s_{\rm switch} - s_{\rm since}|$, i.e. even for a front that has backtracked by a relatively small amount. This follows because the set of liquid saturations adjacent to the backtracking front tend to be associated with much lower mobility than those associated with the original forward propagating front.

As far as the front propagation is concerned, these lower mobilities (reducing total fluid flux and hence front propagation rate), are partly offset by another effect, namely that, for a specified total fluid flux, the backtracking shock tends to move faster than the original forward propagating front would do. This is seen by the ratio between $(f_{l,{\rm rev},0} - f_{l,{\rm fwd}})/(S_{l,{\rm rev},0} - S_{l,{\rm fwd}})$ and $(1 - f_{l,{\rm fwd}})/(1 - S_{l,{\rm fwd}})$ in equation (4.24), this ratio having a value rather larger than unity (see slopes of lines plotted in Figure 3(a) with relevant data given in Table 2). Note also that if the front ever manages to backtrack by further than it originally moved forward, a significant reduction in propagation speed is predicted to occur (see e.g. Figure 5(b)). The relevant ratio in equation (4.25) is that between $f_{l,{\rm rev},\infty}/S_{l,{\rm rev},\infty}$ and $(1 - f_{l,{\rm fwd}})/(1 - S_{l,{\rm fwd}})$ (again see Figure 3(a) and Table 2), which although slightly greater than unity, is not nearly big enough to compensate for the backtracking mobility $M_{\rm tot,rev,\infty}$ being much smaller than $M_{\rm tot,fwd}$.

5. Conclusions

To conclude, equations (4.24)–(4.26) taken together constitute a model for what happens in 2-D pressure-driven growth in situations in which a flow reversal occurs due to a reduction in driving pressure. Under circumstances like these, whereas gas pushes into liquid initially, later on liquid pushes back into gas. In fact only parts of the front at depth undergo the flow reversal. Points higher up on the front (above a "neutral" depth) do not undergo flow reversal, and continue to be described by the original fractional flow equation (4.4), just with a reduced net driving pressure. In realistic oil recovery applications, operations are designed such that most of the oil is likely to be encountered higher up (i.e. above the "neutral depth") so any reverse flow at depth tends to involve other fluids (e.g. water invading foamed gas).

The reverse flow model for 2-D pressure-driven growth associates each point on the 2-D front with local 1-D motion of a shock described by an underlying 1-D fractional-flow theory. Moreover the 2-D model captures key features of the underlying 1-D theory: during reverse flow there is a complex double fan structure either side of a shock, with comparatively low liquid saturations downstream of the shock (these saturations also appear during the forward flow) and comparatively high liquid saturations upstream (saturations that do not appear during forward flow). The lowest mobilities are associated with the higher liquid saturations near the upstream

side of the shock, so it is this side that determines how rapidly fluids (i.e. liquid plus gas) can flow, and hence how fast the 1-D shock or equivalently 2-D front propagates. Even though the 1-D model feeds into the 2-D one, there is (unlike in 1-D) no requirement in the 2-D model for points to retrace the same trajectory during reverse flow as they executed during forward flow.

In this work we have presented equations (4.24)–(4.26) but not attempted to solve them, leaving that task for further work. What we do know is that any material point on the front, tracked to long enough time, should eventually attain the aforementioned "neutral" depth at which its motion stops. The model described by equations (4.24)–(4.26) however indicates how quickly material points evolve towards that final neutral depth. Such evolution might however be less straightforward than is initially apparent. The backtracking portion of the front has a concave shape seen from the direction towards which it is moving. It is already known [41] for the pressure-driven growth model that concavities have the potential to focus down into sharp corners, which physically correspond to regions over which a foam front reorients direction over a distance scale much less than the overall extent of the front. Whether or not this sort of behaviour is prominent when equations (4.24)–(4.26) are solved still remains to be seen.

Another task for further work concerns how well the flow-reversed pressure-driven growth model (4.24)–(4.26) (which assigns dissipative pressure drops entirely to a low mobility foam front) would compare with a simulation based on Darcy's law (which distributes pressure drops over the entire flow domain). The indications from the results presented here are that mobilities at the foam front are even lower in reverse flow mode than in forward flow, a result that follows from having different saturations in forward and reverse flows, even assuming the same underlying fractional flow curve in both situations as has been done here. It follows thereby that agreement between a pressure-driven growth model and a Darcy simulation can be expected to be better in reverse flow than in a forward flow mode.

Nonetheless difficulties remain even in reverse flow mode. We have stated that validity of the pressure-driven growth model assumes the low mobility region at the foam front is thin compared to the distance the front itself displaces. This applies not just in forward flow but in reverse flow also. Indeed in reverse flow the requirement to have a thin front is particularly delicate. Suppose that an arbitrarily thin front is replaced by a small but finite thickness region near the front, and then flow reverses and the system starts to backtrack. Points with different saturations within that small but finite thickness region then start to interact not just with points on the specific path that was executed to reach one particular location on the front (e.g. point C in Figure 2), but also with points (and their corresponding saturations) on neighbouring paths executed to reach neighbouring locations on the front. This represents a considerable complication.

Ethics. This paper does not raise any ethical issues.

Data Accessibility. Programs used to generate results and data obtained from them are supplied as supplementary material.

Authors' Contributions. P. Grassia (PG) suggested the research problem to M. Eneotu (ME), for ME to tackle as part of his PhD project (under PG's supervision). ME conceived the technique for obtaining the solution, and implemented it (albeit, for a set of parameter values different from those reported here). ME wrote up that work as chapters within his PhD thesis. PG then implemented the solution for the actual set of parameter values reported here and assisted with re-drafting ME's written work into journal article format. Both authors approved the final version and agree to be accountable for all aspects the work.

Competing Interests. We declare we have no competing interests.

Funding. M. Eneotu was funded by the Petroleum Technology Development Fund (PTDF), Nigeria.

Acknowledgements. P. Grassia acknowledges useful discussions with I. Frigaard, who (some years ago now) enquired what might happen to pressure-driven growth under flow reversal.

References

1. Lake LW, Johns R, Rossen WR, Pope G. 2014 *Fundamentals of Enhanced Oil Recovery*. Richardson, TX: Society of Petroleum Engineers.
2. Willhite GP. 1986 *Waterflooding*. Richardson, TX: Society of Petroleum Engineers.
3. Green DW, Willhite GP. 1998 *Enhanced Oil Recovery*. Richardson, TX: Society of Petroleum Engineers.
4. Farajzadeh R. 2009 *Enhanced Transport Phenomena in CO_2 Sequestration and CO_2 EOR*. PhD thesis Delft University of Technology.
5. Sorbie KS. 1991 *Polymer-Improved Oil Recovery*. Glasgow: Blackie & Son.
6. Schramm LL, Wassmuth F. 1994 Foams: Basic Principles. In Schramm LL, editor, *Foams: Fundamentals and Applications in the Petroleum Industry* vol. 242 *Advances in Chemistry* pp. 3–45. Washington, DC: American Chemical Society.
7. Kovscek AR, Radke CJ. 1994 Fundamentals of Foam Transport in Porous Media. In Schramm LL, editor, *Foams: Fundamentals and Applications in the Petroleum Industry* vol. 242 *Advances in Chemistry* pp. 115–163. Washington, DC: American Chemical Society.
8. Rossen WR. 1996 Foams in Enhanced Oil Recovery. In Prud'homme RK, Khan SA, editors, *Foams: Theory, Measurements and Applications* Surfactant Science Series pp. 99–187. New York: Marcel Dekker.
9. Farajzadeh R, Andrianov A, Krastev R, Hirasaki GJ, Rossen WR. 2012 Foam-oil interaction in porous media: Implications for foam assisted enhanced oil recovery. *Adv. Coll. Interface Sci.* **183–184**, 1–13. doi.org/10.1016/j.cis.2012.07.002.
10. Cottin C, Bodiguel H, Colin A. 2010 Drainage in two-dimensional porous media: From capillary fingering to viscous flow. *Phys. Rev. E* **82**, 046315. doi.org/10.1103/PhysRevE.82.046315.
11. Géraud B, Jones SA, Cantat I, Dollet B, Méheust Y. 2016 The flow of a foam in a two-dimensional porous medium. *Water Resour. Res.* **52**, 773–790. doi.org/10.1002/2015WR017936.
12. Bertin HJ, Apaydin OG, Castanier LM, Kovscek AR. 1999 Foam flow in heterogeneous porous media: Effect of cross flow. *SPE J.* **4**, 75–82. doi.org/10.2118/56009-PA.
13. Kovscek AR, Bertin HJ. 2003a Foam mobility in heterogeneous porous media. I. Scaling concepts. *Transport in Porous Media* **52**, 17–35. doi.org/10.1023/A:1022312225868.
14. Kovscek AR, Bertin HJ. 2003b Foam mobility in heterogeneous porous media. II. Experimental observations. *Transport in Porous Media* **52**, 37–49. doi.org/10.1023/A:1022368228594.
15. Khatib ZI, Hirasaki GJ, Falls AH. 1988 Effects of capillary pressure on coalescence and phase mobilities in foams flowing through porous media. *SPE Reservoir Engineering* **3**, 919–926. doi.org/10.2118/15442-PA.
16. Falls AH, Hirasaki GJ, Patzek TW, Gauglitz DA, Miller DD, Ratulowski T. 1988 Development of a mechanistic foam simulator: The population balance and generation by snap-off. *SPE Reservoir Engineering* **3**, 884–892. doi.org/10.2118/14961-PA.
17. Kovscek AR, Patzek TW, Radke CJ. 1994 Mechanistic prediction of foam displacement in multidimensions: A population balance approach. In *SPE/DOE Improved Oil Recovery Symposium, Tulsa, OK, 17th–20th April*. doi.org/10.2118/27789-MS.
18. Kovscek AR, Patzek TW, Radke CJ. 1995 A mechanistic population balance model for transient and steady-State foam flow in Boise sandstone. *Chem. Engng Sci.* **50**, 3783–3799. doi.org/10.1016/0009-2509(95)00199-F.
19. Kovscek AR, Patzek TW, Radke CJ. 1997 Mechanistic foam flow simulation in heterogeneous and multidimensional porous media. *SPE J.* **2**, 511–526. doi.org/10.2118/39102-PA.
20. Cheng L, Reme AB, Shan D, Coombe DA, Rossen WR. 2000 Simulating foam processes at high and low foam qualities. In *SPE/DOE Improved Oil Recovery Symposium, Tulsa, OK, 3rd–5th April*. doi.org/10.2118/59287-MS.
21. Kam SI. 2008 Improved mechanistic foam simulation with foam catastrophe theory. *Colloids and Surf. A, Physicochem. and Engg Aspects* **318**, 62–77. doi.org/10.1016/j.colsurfa.2007.12.017.
22. Rossen WR. 2013 Numerical challenges in foam simulation: A review. In *SPE Annual Technical Conference and Exhibition, New Orleans, LA, 30th September–2nd October*. doi.org/10.2118/166232-MS.
23. Ma K, Lopez-Salinas JL, Puerto MC, Miller CA, Biswal SL, Hirasaki GJ. 2013 Estimation of

parameters for the simulation of foam flow through porous media. Part 1: The dry-out effect. *Energy & Fuels* **27**, 2363–2375. doi.org/10.1021/ef302036s.
24. Ma K, Ren G, Mateen K, Morel D, Cordelier P. 2015 Modeling techniques for foam flow in porous media. *SPE J.* **20**, 453–470. doi.org/10.2118/169104-PA.
25. Farajzadeh R, Lotfollahi M, Eftekhari AA, Rossen WR, Hirasaki GJ. 2015 Effect of permeability on implicit-texture foam model parameters and the limiting capillary pressure. *Energy & Fuels* **29**, 3011–3018. doi.org/10.1021/acs.energyfuels.5b00248.
26. Zeng Y, Muthuswamy A, Ma K, Wang L, Farajzadeh R, Puerto M, Vincent-Bonnieu S, Eftekhari AA, Wang Y, Da C, Joyce JC, Biswal SL, Hirasaki GJ. 2016 Insights on foam transport from a texture-implicit local-equilibrium model with an improved parameter estimation algorithm. *Ind. Eng. Chem. Res.* **55**, 7819–7829. doi.org/10.1021/acs.iecr.6b01424.
27. Jiménez AI, Radke CJ. 1989 Dynamic Stability of Foam Lamellae Flowing Through a Periodically Constricted Pore. In Borchardt JK, Yen TF, editors, *Oil-Field Chemistry: Enhanced Recovery and Production Stimulation* number 396 in ACS Symposium Series pp. 460–479. Washington: American Chemical Society.
28. Rossen WR. 1990a Minimum pressure gradient for foam flow in porous media: Effect of interactions with stationary lamellae. *J. Colloid and Interf. Sci.* **139**, 457–468. doi.org/10.1016/0021-9797(90)90118-8.
29. Rossen WR. 1990b Theory of mobilization pressure gradient of flowing foams in porous media: I. Incompressible foam. *J. Colloid and Interf. Sci.* **136**, 1–16. doi.org/10.1016/0021-9797(90)90074-X.
30. Rossen WR. 1990c Theory of mobilization pressure gradient of flowing foams in porous media: III. Asymmetric lamella shapes. *J. Colloid and Interf. Sci.* **136**, 38–53. doi.org/10.1016/0021-9797(90)90076-Z.
31. Cox SJ, Neethling S, Rossen WR, Schleifenbaum W, Schmidt-Wellenburg P, Cilliers JJ. 2004 A theory of the effective yield stress of foam in porous media: The motion of a soap film traversing a three-dimensional pore. *Colloids and Surf. A, Physicochem. and Engg Aspects* **245**, 143–151. doi.org/10.1016/j.colsurfa.2004.07.004.
32. Ferguson DJ, Cox SJ. 2013 The motion of a foam lamella traversing an idealised bi-conical pore with a rounded central region. *Colloids and Surf. A, Physicochem. and Engg Aspects* **438**, 56–62. doi.org/10.1016/j.colsurfa.2013.02.015.
33. Nonnekes LE, Cox SJ, Rossen WR. 2015 Effect of gas diffusion on mobility of foam for enhanced oil recovery. *Transp. Porous Media* **106**, 669–689. doi.org/10.1007/s11242-014-0419-z.
34. Shi JX, Rossen WR. 1998 Improved surfactant-alternating-gas foam process to control gravity override. In *Improved Oil Recovery Symposium, Tulsa, OK, 19th–22nd April*. doi.org/10.2118/39653-MS.
35. Shi JX. 1996 *Simulation and Experimental Studies of Foam for Enhanced Oil Recovery*. PhD thesis University of Texas at Austin.
36. Rossen WR, van Duijn CJ, Nguyen QP, Shen C, Vikingstad AK. 2010 Injection strategies to overcome gravity segregation in simultaneous gas and water injection into homogeneous reservoirs. *SPE J.* **15**, 76–90. doi.org/10.2118/99794-PA.
37. de Velde Harsenhorst RM, Dharma AS, Andrianov A, Rossen WR. 2014 Extension and verification of a simple model for vertical sweep in foam SAG displacements. *SPE Reservoir Evaluation & Engg* **17**, 373–383. doi.org/10.2118/164891-PA.
38. Boeije CS, Rossen WR. 2014 Gas injection rate needed for SAG foam processes to overcome gravity override. *SPE J.* **20**, 49–59. doi.org/10.2118/166244-PA.
39. Zeng Y, Farajzadeh R, Biswal SL, Hirasaki GJ. 2019 A 2-D simulation study on CO_2 soluble surfactant for foam enhanced oil recovery. *J. Ind. Eng. Chem.* **72**, 133–143. doi.org/10.1016/j.jiec.2018.12.013.
40. Shan D, Rossen WR. 2004 Optimal injection strategies for foam IOR. *SPE J.* **9**, 132–150. doi.org/10.2118/88811-PA.
41. Grassia P, Mas-Hernández E, Shokri N, Cox SJ, Mishuris G, Rossen WR. 2014 Analysis of a model for foam improved oil recovery. *J. Fluid Mech.* **751**, 346–405. doi.org/10.1017/jfm.2014.287.
42. Grassia P, Lue L, Torres-Ulloa C, Berres S. 2017 Foam front advance during improved oil recovery: Similarity solutions at early times near the top of the front. *J. Fluid Mech.* **828**, 527–572. doi.org/10.1017/jfm.2017.541.
43. Zhou ZH, Rossen WR. 1995 Applying fractional-flow theory to foam processes at the

'limiting capillary pressure'. *SPE Advanced Technology Series* **3**, 154–162. doi.org/10.2118/24180-PA.
44. Rossen WR, Zeilinger SC, Shi JX, Lim MT. 1999 Simplified mechanistic simulation of foam processes in porous media. *SPE J.* **4**, 279–287. doi.org/10.2118/57678-PA.
45. Dholkawala ZF, Sarma HK, Kam SI. 2007 Application of fractional flow theory to foams in porous media. *J. Petrol. Sci. Eng.* **57**, 152–165. doi.org/10.1016/j.petrol.2005.10.012.
46. Ashoori E, van der Heijden TLM, Rossen WR. 2010 Fractional-flow theory of foam displacements with oil. *SPE J.* **15**, 260–273. doi.org/10.2118/121579-PA.
47. Afsharpoor A, Lee GS, Kam SI. 2010 Mechanistic simulation of continuous gas injection period during surfactant-alternating-gas (SAG) processes using foam catastrophe theory. *Chem. Engng Sci.* **65**, 3615–3631. doi.org/10.1016/j.ces.2010.03.001.
48. Mas-Hernández E, Grassia P, Shokri N. 2016 Modelling foam improved oil recovery within a heterogeneous reservoir. *Colloids and Surf. A, Physicochem. and Engg Aspects* **510**, 43–52. doi.org/10.1016/j.colsurfa.2016.07.064.
49. Grassia P, Torres-Ulloa C, Berres S, Mas-Hernández E, Shokri N. 2016 Foam front propagation in anisotropic oil reservoirs. *Eur. Phys. J. E* **39**, 42. doi.org/10.1140/epje/i2016-16042-5.
50. Grassia P. 2017 Foam front displacement in improved oil recovery in systems with anisotropic permeability. *Colloids and Surf. A, Physicochem. and Engg Aspects* **534**, 44–51. doi.org/10.1016/j.colsurfa.2017.03.059.
51. Mas-Hernández E, Grassia P, Shokri N. 2015a Foam improved oil recovery: Foam front displacement in the presence of slumping. *Colloids and Surf. A, Physicochem. and Engg Aspects* **473**, 123–132. doi.org/10.1016/j.colsurfa.2014.12.023.
52. Mas-Hernández E, Grassia P, Shokri N. 2015b Foam improved oil recovery: Modelling the effect of an increase in injection pressure. *Eur. Phys. J. E* **38**, 67. doi.org/10.1140/epje/i2015-15067-6.
53. Lotfollahi M, Farajzadeh R, Delshad M, Varavei A, Rossen WR. 2016 Comparison of implicit-texture and population-balance foam models. *J. Nat. Gas Sci. Eng.* **31**, 184–197. doi.org/10.1016/j.jngse.2016.03.018.
54. Brooks RH, Corey AT. 1964 Hydraulic properties of porous media. Technical report Hydrology Papers, Colorado State University.
55. Corey AT. 1954 The interrelation between gas and oil relative permeabilities. *Prod. Monthly* **19**, 38–41.
56. Persoff P, Radke CJ, Pruess K, Benson SM, Witherspoon PA. 1991 A laboratory investigation of foam flow in sandstone at elevated pressure. *SPE Reservoir Engg* **6**, 365–372. doi.org/10.2118/18781-PA.
57. Rossen WR, Boeije CS. 2015 Fitting foam-simulation-model parameters to data: II. Surfactant-alternating-gas foam applications. *SPE Reservoir Evaluation & Engg* **18**, 273–283. doi.org/10.2118/165282-PA.
58. Gauglitz PA, Friedmann F, Kam SI, Rossen WR. 2002 Foam generation in homogeneous porous media. *Chem. Engng Sci.* **57**, 4037–4052. doi.org/10.1016/S0009-2509(02)00340-8.
59. Buckley SE, Leverett MC. 1942 Mechanism of fluid displacements in sands. *Trans. AIME* **146**, 107–116. doi.org/10.2118/942107-G.
60. Courant R, Friedrichs KO. 1948 *Supersonic Flow and Shock Waves*. New York: Interscience.
61. Zhou ZH, Rossen WR. 1994 Applying fractional-flow theory to foams for diversion in matrix acidization. *SPE Prod. Facil.* **9**, 29–35. doi.org/10.2118/24660-PA.
62. Gong J, Flores Martinez W, Vincent-Bonnieu S, Bahrim RZK, Mamat CANBC, Tewari RD, Amir MIM, Farajzadeh R, Rossen W. 2020 Effect of superficial velocity on liquid injectivity in SAG foam EOR. Part 2: Modelling. *Fuel* **279**, 118302. doi.org/10.1016/j.fuel.2020.118302.